Title
Decoding the Relationship between Composition and Various Properties of Calcium Silicate and Calcium Aluminosilicate Glasses

Author
Hu, Yushu

Publication Date
2020

Peer reviewed|Thesis/dissertation

UNIVERSITY OF CALIFORNIA

Los Angeles

Decoding the Relationship between Composition and Various Properties of Calcium Silicate and Calcium Aluminosilicate Glasses

A dissertation submitted in partial satisfaction of the

requirements for the degree Master of Science

in Materials Science and Engineering

by

Yushu Hu

2020

ABSTRACT OF THE DISSERTATION

Decoding the Relationship between Composition and Various Properties

of Calcium Silicate and Calcium Aluminosilicate Glasses

by

Yushu Hu

Master of Science in Materials Science and Engineering

University of California, Los Angeles, 2020

Professor Gaurav Sant, Chair

This dissertation contributes to decode the relationship between glass composition and various properties that are crucial to novel glass design by performing molecular dynamics simulations. The topics include the prediction of glass transition temperature, the origin of glass-forming ability, and the impact of cooling rate on glass relaxation.

In general, the first two properties are analyzed by utilizing topological constraint theory. By combining molecular dynamics simulations and topological constraint theory, a fully analytical model is developed to predict the fictive glass transition temperature of $(CaO)_x(SiO_2)_{1-x}$ glass system. To be specific, this model takes composition as input and provides the prediction of glass transition temperature as output.

On the other hand, glass-forming ability is an important factor that guides the manufacturing process while sometimes imposes limitations to glass engineering. Despite many empirical successes to identify and characterize glass-forming ability in various glass systems, there exists a lack of knowledge of physical details in the glass structure. Here, we conduct molecular dynamics simulations of a series of calcium silicate glasses. We show that the flexible-to-rigid topological transition coincides with the compositional window that has optimal glass-forming ability. By explaining this transition from the aspect of internal flexibility and internal stress within the network, we aim to provide an alternative topological explanation for the nature of glass-forming ability.

Chapter 3 is a reprint of a previously published journal article. It demonstrates the impact of cooling rate on glass transition by analyzing glass relaxation and hysteresis of a series of silicate glasses. It proves that by extrapolating simulation data, one can access the results that are close to those generated from experimental cooling rates.

The dissertation of Yushu Hu is approved.

Mathieu Bauchy

Jaime Marian

Amartya Sankar Banerjee

Gaurav Sant, Committee Chair

University of California, Los Angeles

2020

To my beloved family and my cutest feline buddy QB

TABLE OF CONTENTS

LIST OF FIGURES

LIST OF TABLES

Chapter 1 Topological Model for $(CaO)_x(SiO2)_{1-x}$ Glasses: Prediction of Glass Transition Temperature

1.1 Introduction

Silicate glasses have been extensively studied throughout glass technology and materials science as they are ubiquitous in nature (i.e., Earth's mantle, magmas, etc.)[1,2]. The addition of alkali cations, such as Na+, Ca2+, etc., into the silicate network has been shown to modify their properties, which advance their application in many fields. For example, substrates for displays[3], optical discs, bioactive glasses[4], cement hydrates[5], etc. Among them, binary alkali silicate glasses have gained attention mainly due to their simplicity and technological relevance[2,6].

Among various glass properties, the glass transition temperature is directly linked to viscosity, hence making it an important factor for glass manufacturing process and for understanding the glass transition and relaxation[7]. Mauro and his collogues developed the Yue-Ellison-Gupta-Allan (MYEGA) equation[8], which directly describes the relationship between glass transition temperature (Tg), fragility (m) and the infinite temperature viscosity (η_∞).

$$log_{10}\eta(T) = log_{10}\eta_\infty + (12 - log_{10}\eta_\infty)\frac{T_g}{T}exp\left[\left(\frac{m}{12 - log_{10}\eta_\infty} - 1\right)\left(\frac{T_g}{T} - 1\right)\right] \quad \text{Eq. 1}$$

T_g and m are input parameters, and studies suggest that η_∞ is a constant due to the fact that all constraints are supposedly broken at infinite high temperature. As a result, the viscosity of the

liquid reaches a limit ultimately. In conclusion, the full behavior of the viscosity-temperature relationship can be predicted with the input of T_g and m. A recent study is focused on $(Bi_2O_3)_x(NaPO3)_{1-x}$ glasses by applying this equation, and it successfully predicts the glass transition temperature and the fragility of the system[9] .

The fragility of the system can be essentially defined by the topological constraint environment of the system, which is linked to glass composition. This idea was first introduced by Phillips' topological constraint theory (TCT) (**Figure 1. 1)**, which will be elaborated in the following sections[10]. His theory was later improved mathematically by the joining effort from Thorpe to connect glass topology with various compositional-dependent glass properties at zero temperature[11–13]. Their work was then extended by Mauro and Gupta[14,15], as they studied the effect of temperature on constraints and hence their contribution to different glass properties (i.e., T_g, m and hardness).

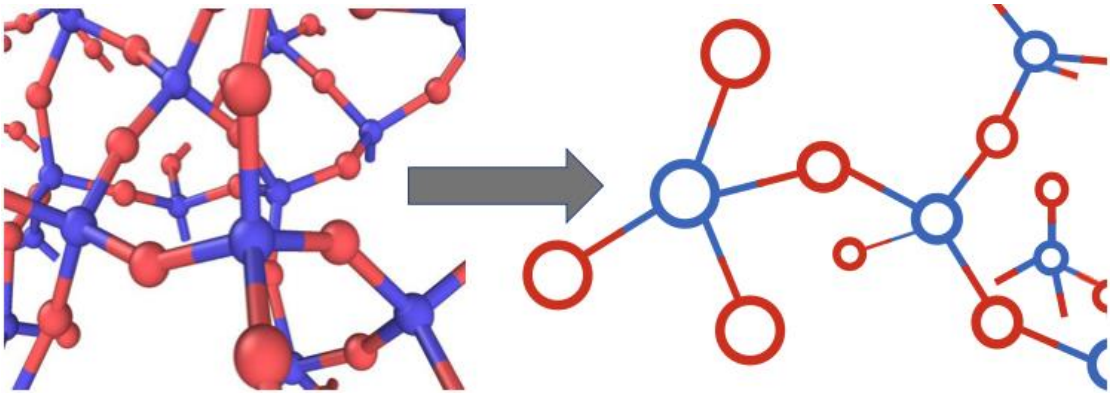

Figure 1. 1 Topological constraint theory has the advantage of simplifying complex disordered atomic networks into mechanical trusses made of nodes (atoms) that are connected to each other by constraints (chemical bonds).

Despite studies carried out to understand the glass transition for calcium silicate (CS) systems[16], a fully analytical model is always desired to predict the glass transition temperature with the input of composition. As for now, the prediction of T_g utilizing the MYEGA relationship has not been applied to many other glass systems. In addition, according to Eriksson and Pelton[17], some composition ranges of the binary CS glasses have poor glass-forming ability. To be specific, high alkali content could cause phase separation, whereas low content results in a liquidous that is extremely high for glass to form. With the difficulty mentioned above, MD simulation has its advantage to take into place instead of carrying out experiments, especially for certain compositions. MD simulations enable us to capture the topology environment of the glass network, while at the same time eliminate the limitations caused by glass-forming ability.

The goal of this work is to build a fully analytical model that predicts the glass transition temperature of CS glasses with the input of composition only, which allows direct access in the future without doing further MD simulations. For simplicity, we first perform MD simulations of a series of $(CaO)_x(SiO_2)_{1-x}$ glasses and calculate their glass transition temperatures. Note that due to the nature of simulations (with a high cooling rate of 100 K/ps), the T_g mentioned in this paper is fictive. Then, we analyze the structural environment by utilizing topological constraint theory and determine the onset temperature of each constraint that contributes to the rigidity of the network. Finally, by investigating the relationship between topological constraints and T_g, we are able to build a topological model that provides good predictions of the fictive glass transition temperature.

1.2 Theory

1.2.1 Topological Constraint Theory

The idea of applying topology to amorphic glassy systems is based on the concept of mechanical stability by Maxwell-Lagrange[18]. In general, mechanical trusses can be described as in the following states of rigidity: flexible (with insufficient constraints), stressed-rigid (overconstrained), or isostatic (with exactly the right amount of constraints). To determine the state of rigidity of a specific truss, one can compare the number of mechanical constraints (N_c) with the number of degrees of freedom of the nodes connecting the trusses. As demonstrated in **Figure 1. 2**, N_c can be determined by counting the number of red sticks. In three-dimensional systems, since there are three translation directions per node, the initial number of degrees of freedom is $3N$, with N being the number of nodes. Similarly, for a rigid structure viewed as a whole, there are six macroscopic degrees of freedom, which include three translation and three rotation directions. Note that nodes are considered as points for simplicity, so the rotation directions are not included. As a result, the remaining degrees of freedom after comparing can be viewed as floppy modes, F , which are then given by:

$$F = 3N - N_c - 6 \qquad \text{Eq. 2}$$

The concept of F can be understood as the internal modes of deformation of a system, where each constraint N_c removes one internal degree of freedom and thus prevents one mode of deformation. That being said, the state of rigidity of a mechanical truss can be identified by assessing F. The network is considered as: (i) flexible, if $F > 0$, (ii) stressed-rigid, if $F < 0$, or (iii) isostatic, if $F = 0$. To be specific, flexible networks have a number of internal modes of

deformation which make them prone to be structurally altered even without the existence of external energy. However, stressed-rigid and isostatic trusses are fully rigid. Thus external energy is necessary to change their structure. Moreover, for stressed-rigid trusses, all constraints cannot be satisfied at the same time. Instead, some of the constraints are under tension while others are under compression, which leads to the formation of internal eigenstress stress. Since all constraints mutually compensate each other, there is no effect on the macroscopic stress of the stressed-rigid trusses. In **Figure 1. 3**, isostatic structure has the ideal state where there is neither internal modes of deformation nor eigenstress.

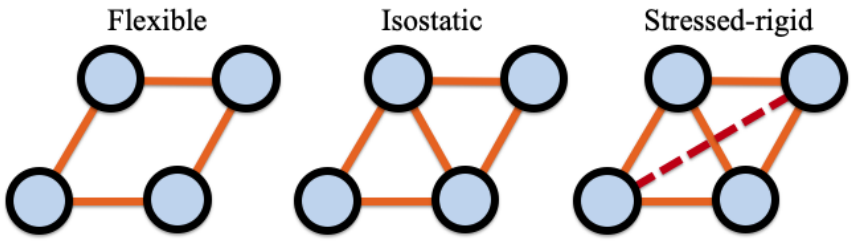

Figure 1. 2 The three states of rigidity of a mechanical network. The dashed red line shows a redundant constraint that is under tension.

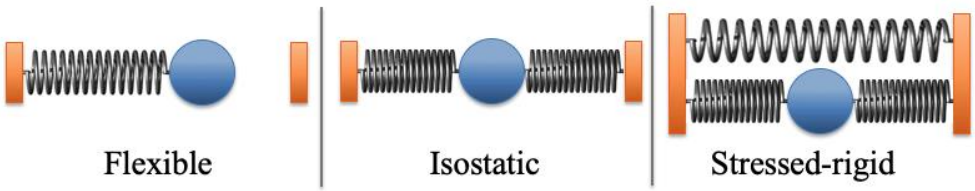

Figure 1. 3 The demonstration of the internal eigenstress that is present in stressed-rigid structures.

1.2.2 Applying Topological Constraint Theory to Glass Systems

The topological constraint theory used for glass systems was first introduced by Phillips in 1979[10], where he applied the Maxwell-Lagrange mechanical stability framework to amorphous glassy networks. This prototype was then refined mathematically by Thorpe in 1983[11]. The application is based on the analogy between mechanical trusses and atomic networks. Specifically, atoms can be considered as nodes that are connected to each other by some constraints. Each constraint serves to prevent the relative atomic motions and remove internal modes of deformation (or internal degrees of freedom). As shown in **Figure 1. 4**, only short-range interactions are considered, which include two kinds of constraints: (i) the radial 2-body bond-stretching (BS) constraints that fix the inter-atomic distances around their average values, and (ii) the angular 3-body bond-bending (BB) constraints that fix angles.

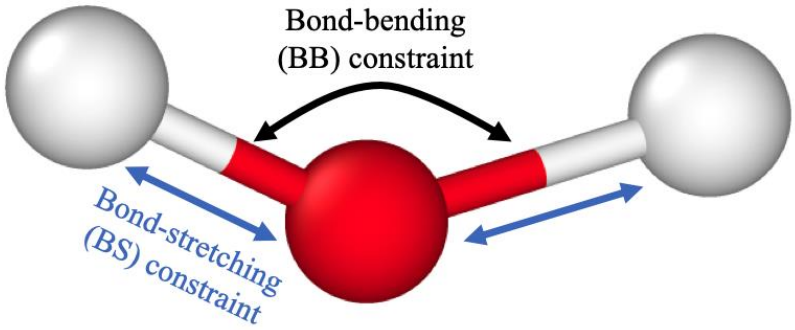

Figure 1. 4 The illustration of the radial bond-stretching (BS) and angular bond-bending (BB) constraints. BS constraints fix interatomic distances, and BB constraints fix interatomic angles.

In covalent networks, all constraints are intact and the number of them only depends on the coordination number (r) of each associated atom. Hence the linear and angular constraints can be calculated as follows:

$$n_{BS} = \frac{1}{2}\, r|_{r\geq 2} \qquad \text{Eq. 3}$$

$$n_{BB} = (2r - 3)|_{r\geq 2} \qquad \text{Eq. 4}$$

To specify, for each atom, a BS constraint is shared by two atoms, so the number of BS constraints is given by $r/2$. While for BB constraints, since any combination of three atoms has one BB constraint inherently and two new constraints are need to fix the position of one additional neighbor, the number of BB constraints is given by $2r - 3$ for $r \geq 2$. It is assumed that atoms with $r = 1$ do not have any BB constraints. With the assumption that all N atoms have a coordination number larger or equal to two, we can calculate the total number of constraints N_c as follows:

$$N_c = \sum_i \left[N_i(\frac{r_i}{2} + 2r_i - 3)\right] = \sum_i \left(N_i \frac{5r_i}{2}\right) - 3N \qquad \text{Eq. 5}$$

N_i is the number of atoms having a coordination number of r_i. With this equation, one can calculate the number of internal degrees of freedom F and thus assess the rigidity of the glass system.

However, it is mathematically more convenient to apply the mean-field approximation in this case, since there is a huge amount of atoms within glasses. By looking at the average number of internal degrees of freedom per atom, $f = F/N$, one can have the follows:

$$f = 3 - n_c - \frac{6}{N} = 3 - n_c \qquad \text{Eq. 6}$$

where $n_c = N_c / N$ *is the average number of constraints per atom*. Here 6 / N can be ignored because this term tends to be infinitely small when N is large enough (i.e., there is a large number of atoms within the atomic network). By applying the same concept, the n_c can also be written as follows:

$$n_c = \sum_i \left[x_i \frac{5r_i}{2} \right] - 3 \qquad \text{Eq. 7}$$

where $x_i = N_i / N$ is the fraction of atoms that have a coordination number r_i.

Similarly, the rigidity of glass systems can be thus determined by assessing f based on the mechanical stability theory of Maxwell-Lagrange. Glasses are considered as: (i) flexible, if $f > 0$ (i.e., $n_c < 3$), (ii) stressed-rigid, if $f < 0$ (i.e., $n_c > 3$), or (iii) isostatic, if $f = 0$ (i.e., $n_c = 3$). With the same spirit, flexible glasses have some internal modes of deformation, and the number of floppy modes per atom is calculated by $f = 3 - n_c$[19–22]. On the other hand, stressed-rigid glasses exhibit internal stress as the result of mutually dependent constraints, and the number of excess

constraints per atom is given by n_c – 3. Isostatic glasses are in the "ideal state" where there are neither floppy modes nor internal stress[5,23].

Then a simplified version to describe glass rigidity can be given in terms of the average coordination number <*r*> as follows:

$$< \mathrm{r} >= \sum_i x_i r_i \qquad \text{Eq. 8}$$

with which the previous equation of n_c can be then expressed as:

$$n_c = \frac{5 < r >}{2} - 3 \qquad \text{Eq. 9}$$

By assuming all BS and BB constraints are intact and all atoms within the network have a coordination number larger or equal to 2, we can conclude that for an isostatic network, where n_c = 3, the average number of coordination number <*r*> = 2.4.

1.2.3 Topology Dependent Glass Transition Temperature

To build an analytical model with the input of composition-dependent constraints and the output of temperature, the quantitative structural details are needed. First, we need the actual mole fraction of each species within the glass system. That being said, we are then able to assess the contribution to the network rigidity of each species, and thus calculate the number of constraints of each species based on TCT. On the other hand, it is also necessary to determine the onset temperature of each constraint, which is the temperature at which each constraint breaks. The

onset temperatures can be calculated by investigating the angular excursion of the corresponding constraint.

The combination of Adam-Gibbs theory[24] and the work of Naumis[25,26] provides a way to define the relationship between glass transition temperature, T_g, and the number of constraints per atom, n_c, as follows:

$$\frac{T_g(x)}{T_g(x_{ref})} = \frac{f[T_g(x_{ref}), x_{ref}]}{f[T_g(x), x]} = \frac{d - n_c[T_g(x_{ref}), x_{ref}]}{d - n_c[T_g(x), x]} \quad \text{Eq. 10}$$

where x is the composition of the CS glass in the fully analytical model, x_{ref} is the composition of the chosen reference, f is the internal degrees of freedom, n_c is the number of constraints per atom, and d is the dimensionality of the network.

1.2.4 Simulation Details

We first simulate a series of calcium silicate glasses $(CaO)_x(SiO_2)_{1-x}$ within the range of $x = 0 \sim 80\%$ by molecular dynamics. The potential used to simulate the CS glasses was developed by Jakse *et al*[3]. This interatomic potential relies on fixed partial charges and a simple two-body Buckingham potential formulation. A timestep of 1 fs is used and the Coulombic interactions are evaluated with the Ewald summation method, with a convergence criterion factor of 10^{-5}[, 27–33]. For the short-range and Coulombic interactions, the cutoffs are 8 and 12 Å[34], respectively. This potential was demonstrated to provide a sound description of the structural and elasticity properties of CS glasses[35]. When preparing the melts using LAMMPS package[36], the

initial liquid configurations are generated by randomly allocating around 3000 atoms in a cubic simulation box, while at the same time avoiding any unrealistic overlap. Then the system is equilibrated at 3000 K for 100 ps in *NVT* ensemble to ensure the loss of the memory of the initial configurations. Following that, the system is relaxed at 3000 K in *NPT* ensemble (under zero pressure) for another 100 ps. Then the glass is ready to be cooled at the rate of 1 K/ps from 3000 K to room temperature, 300 K, with the cooling increment of 100 K during temperature decrease. Finally, the system is subjected to a final relaxation by staying at room temperature for 100 ps.

1.3 Structure

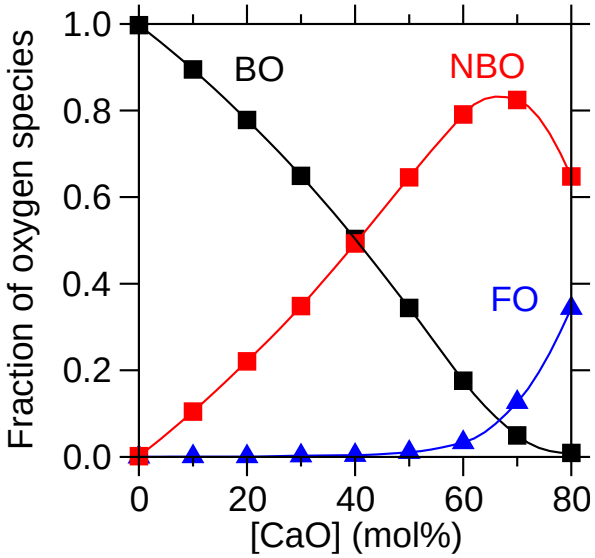

Figure 1. 5 Fractions of different types of oxygen atoms as a function of [CaO] mol%. BO: bridging oxygen, which connects two Si atoms; NBO: non-bridging oxygen, which connects one Si atom and one Ca atom; FO: free oxygen, connected with and only with at least two Ca atoms. The solid lines serve as a guide to the eye.

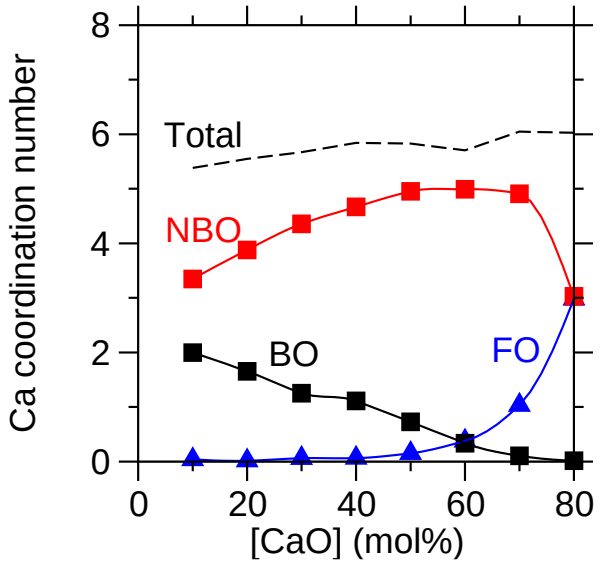

Figure 1. 6 The average coordination number of all Ca atoms as a function of [CaO] mol%. The contributions of BO, NBO, and FO are also demonstrated, which is in accordance with the observation in Figure 1. 5. The lines serve as a guide to the eye.

In order to do constraints enumeration, we first focus on the identification of the atomic structures within the CS glasses simulated. As shown in **Figure 1. 5**, as more CaO content is added to the system, the number of BO decreases and the number of NBO increases. This is expected since theoretically, each Ca atom added to the system would create two NBOs. However, what is not predicted is the formation of FO, which dramatically increases starting at [CaO] mol% = 70 %. The formation of FO is due to the fact that an added Ca atom does not necessarily consume a BO first. Instead, it can possibly connect to an NBO, thus creating an FO. This has a higher possibility to happen when the concentration of CaO is relatively higher or when the system is almost saturated with glass modifier, where there are significantly more NBOs than BOs.

We then look at the Ca coordination number and the contributions coming from different oxygen species to further access the structural details of the glasses. **Figure 1. 6** presents the average Ca coordination number together with the contributions. The coordination number that comes from all oxygen species in total has a steady distribution and is always around 6, which yields expected result as it is the usual coordination number of Ca in a crystal lattice. On the other hand, the contributions coming from BO, NBO and FO all share the same trend as that of the fraction of different species in **Figure 1. 5**. Both analyses yield expected structural details, which show the validity of applying TCT in this glass system and lay a sound foundation for constraints enumeration of the system.

1.4 Topological Model for Glass Transition Temperature

1.4.1 Counting Constraints Based on the Relative Motion between Atoms

When it comes to interatomic interaction measurements, it is desirable if a direct computation of the bonding energy between atoms (pairs or triplets) can be conducted. However, it is more convenient to track the relative motion between atoms where we look at the "consequence" instead of the "cause" of topological constraints[37–39] .

The analysis of the interatomic motion can be viewed as proving the existence of constraints that are preventing such motions. Similarly, this kind of "reverse" analysis is often used, for example, analyzing the parabolic trajectory of a projectile to infer the magnitude of gravity. This idea is based on the fact that both BS and BB constraints serve to maintain the interatomic distance or

angles and keep them at their average values, as shown in **Figure 1. 7**. That being said, subtle interatomic motions suggest strong constraints, whereas strong interatomic motions infer weak constraints or even the lack of constraints. This way of counting constraints has been successfully applied to chalcogenide and oxide glasses[38–44] and to atomic-scale models of cement hydrates[5,45,46].

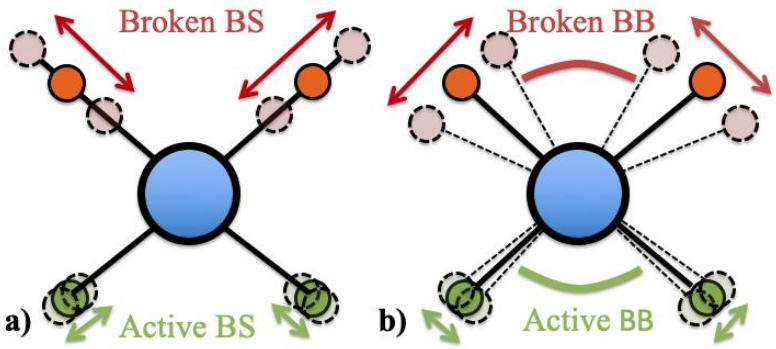

Figure 1. 7 Illustration of the analysis of the topological constraints by measuring the relative motion between atoms with MD simulations. **(a)** Radial bond-stretching and **(b)** angular bond-bending constraints per atom.

1.4.2 Enumeration of Bond-Bending Constraints

We then focus on the analysis of the Si-O-Si and O-Si-O BB constraints. For a central atom 0, we first determine its N nearest neighbors, and they form $N(N\text{-}1)/2$ independent angles around it (i.e., 102, 103, 104, 203, etc.). Then we track the value of each angle over time to compute the (i) average angle θ and (ii) standard deviation σ_θ of each angle. The concept of σ_θ is defined as the angular excursion (with the unit in degree) of each angle formed with the central atom 0. After that, we are able to calculate the relative angular excursion of each angle as σ_θ / θ (with the unit

in %). This methodology is proved to show a clear gap between the relative angular excursion of intact and broken constraints for both BS and BB constraints. Even though the choice of threshold does not significantly matter due to the clear gap, a threshold around 7% typically gives good results[38,47], which is also in accordance with the Lindemann criterion[48]. Note that the exact value of this threshold of relative angular excursion may depend on the choice of forcefield.

1.4.3 Effect of Temperature on Topological Constraints

As mentioned earlier in **Theory** section, each constraint has certain free energy, and eventually breaks as temperature increases. In order to build a temperature-dependent topological model, it is necessary to assess the onset temperature at which each contributing constraint breaks [14,15,49]. With this information, we can then analyze the fraction of intact and broken constraints, respectively, as a function of temperature[38].

The previously explained methodology of calculating angular excursion could be utilized and extended to track the effect of temperature on topological constraints. To be specific, we track the relative angular excursion of the contributing constraints as a function of temperature, which yields a distribution of the relative angular excursion for each constraint at each temperature. **Figure 1. 8** demonstrates this distribution of the relative angular excursions of Si-O-Si and O-Si-O bond-bending constraints in a $(CaO)_{50}(SiO_2)_{50}$ glass. Note that for each Si atom, there are 4 O-Si-O angles; and for each BO, there is 1 Si-BO-Si angle. From the distributions, we found that the relative angular constraints around Si atoms are lower than that around BO atoms, which is in

accordance with the fact that intrapolytope (inside the SiO_4 polytopes) BB constraints are stronger than interpolytope (between the SiO_4 polytopes) BB constraints[14,38]. Also, we note that both of the distributions gradually shift toward larger values of relative angular excursion as temperature increases. This trend infers that BB constraints start to become intact with an increasing temperature.

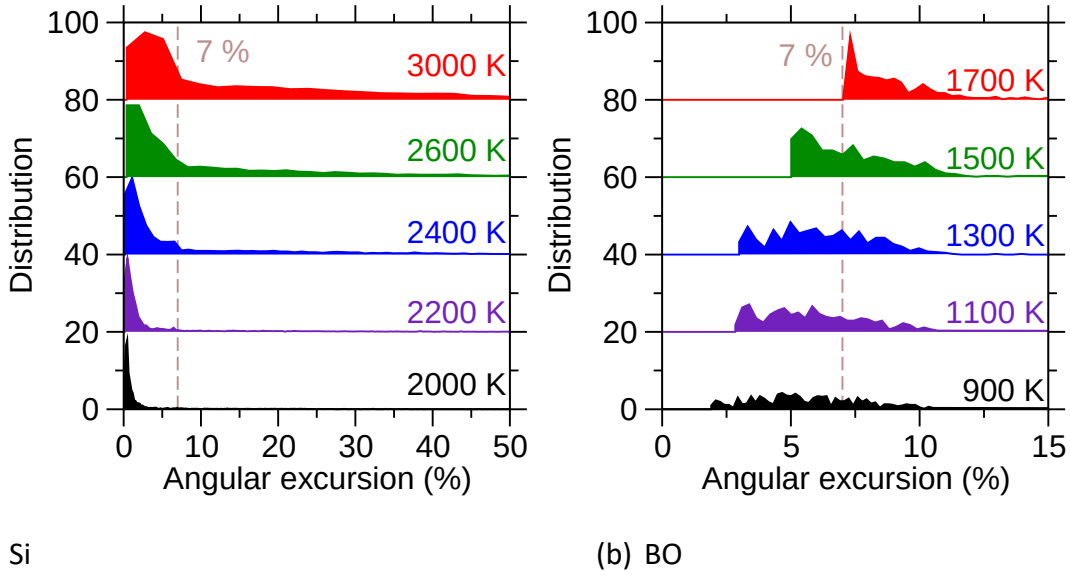

Figure 1. 8 Distributions of relative angular excursions of the angles forming around **(a)** Si atoms (i.e., 4 O-Si-O angles) and **(b)** BO atoms (i.e., 1 Si-BO-Si angle) in a $(CaO)_{50}(SiO_2)_{50}$ glass.

Despite the commons, there are some noticeable differences between the behaviors of the two BB constraints as well as temperature increases. First of all, for O-Si-O BB constraints, the position where the distribution is at its maximum only shifts moderately toward larger values of relative angular excursion upon increasing temperature. Meanwhile, the distributions show long tails extending toward very large value of relative angular excursion. This reflects that a large portion of BB constraints remains relatively unaffected as temperature increases, with a fraction

of them break dramatically as shown by the long tail. This pattern can be well explained by a previous work showing that for each Si atom, the BB constraints associated with the fourth O neighbor (i.e., angles 104, 204 and 304) are the first to break, and the rest remain intact even until very high temperature[38]. Different from that, the distributions of the Si-BO-Si BB constraints gradually shift as a whole toward larger values as temperature increases. This suggests that BB constraints collectively break as temperature increases. In general, the distributions of the relative angular excursion combined with the 7% threshold mentioned earlier allow us to determine the fraction of intact and broken constraints respectively.

In addition, the onset temperature of each constraint can also be calculated from the relative angular excursion. **Figure 1. 9** is generated by taking the average of the relative angular excursion at each temperature and plotting as a function of temperature for each constraint. In general, the average relative angular excursions of Si-BO-Si and O-Si-O BB constraints both show a bilinear behavior. They are almost constant at lower temperatures, and they linearly increase at higher temperatures. Again, the onset temperature can be determined by looking at the 7% threshold, which is the temperature at which the constraint has its average relative angular excursion crosses the threshold. The analysis gives us the two onset temperatures for Si-BO-Si and O-Si-O BB constraints: T_1 = 1350 K and T_2 = 2250 K. The result is in accordance with the previous analysis that O-Si-O BB constraints are strong than Si-BO-Si BB constraints and thus can sustain higher onset temperature before they break.

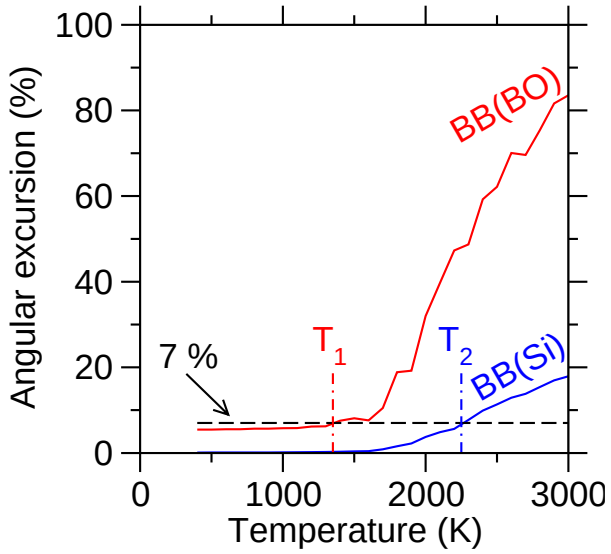

Figure 1. 9 Average relative angular excursions associated with the bond-bending BB constraints around Si atoms and BO atoms, respectively (i.e., O-Si-O and Si-BO-Si), as a function of temperature. The horizontal line indicates the threshold of relative angular excursion (7%) defining intact (< 7%) and thermally-broken (> 7%) constraints.

1.4.4 Analytical Model

In order to build an analytical model that can predict the glass transition temperature with topological constraints, it is necessary to know the topology of the network. Here in **Table 1**, we present our calculation of constraints per atom within the CS network.

Table 1 Analytical calculation of constraints per atom.

	fraction	CN	BS	BB	BS+BB
Ca	x	5	5	0	5
O	2-x	\	\	\	\
BO	2-3x	2	\	1	1
NBO	2x	1	\	0	0
Si	1-x	4	4	5	9

The analytical model is based on several basic assumptions. Firstly, the fraction of each element is calculated based on the hypothesis that each Ca atom creates two NBO atoms. Since the fraction of Ca, Si and O atoms are known according to $(CaO)_x(SiO_2)_{1-x}$, we can simply assume the fraction of NBO is twice the fraction of Ca atoms. Based on that, we further assume that there are only two types of O atoms, BO and NBO (no FO), which supports the formula: BO = O – NBO. Secondly, when establishing the coordination number (CN) of each element, for Ca atoms, it is assumed that their local environment of oxygen atoms would always obey CN_Ca-O = 5. Note that we assume there is no BB constraint of Ca atoms, given that their angular configuration is not clearly defined. On the other hand, for Si atoms, it is agreed that the Si tetrahedra are very stable, hence CN_Si-O = 4. Thirdly, in general, all BS constraints are fully attributed to cations, i.e. Ca and Si atoms, while there is no limitation applied to BB constraints. The number of BS constraints is determined according to r, the CN of each element, while the number of BB constraints complies with the following formula: $n_{BB} = 2r - 3$ (Eq.4).

With that said, the calculation of the n_c of the simulated glasses is demonstrated in **Table 1** and the resulting analytical model of n_c is the following equation:

$$n_c = \frac{11 - 7x}{3 - x} \quad \text{Eq. 11}$$

Note that the analytical model terminates at $x = 0.67$, $n_c = 2.71$, where all BO are consumed by the added Ca atoms, and the assumptions no longer hold true. At that point, all oxygen atoms are considered as NBO.

With the above information, we are able to calculate the contribution of each constraint in the network in the form of number of constraints, n_c. Note that there are four constraints that contribute to the system based on our assumptions: Si_BS, Si_BB, Ca-NBO_BS and BO_BB constraints.

$$n_{c,Si\_BS}(x) = \frac{4 - 4x}{3 - x} \quad \text{Eq. 12}$$

$$n_{c,Si\_BB}(x) = \frac{5 - 5x}{3 - x} \quad \text{Eq. 13}$$

$$n_{c,Ca-NBO\_BS}(x) = \frac{5x}{3 - x} \quad \text{Eq. 14}$$

$$n_{c,BO\_BB}(x) = \frac{2 - 3x}{3 - x} \quad \text{Eq. 15}$$

By applying **Eq.10** with the above number of constraints, we are able to get the predicted glass transition temperature as a function of the glass composition. Note that the glass transition temperature of $(CaO)_{20}(SiO_2)_{80}$ was chosen as the reference T_g (with x = 20%). The predicted $T_g(x)$ is plotted together with the T_g from MD simulations in **Figure 1. 10(a)**. In general, the model well predicts the simulated T_g, namely they both decrease upon the increase of CaO content, with plateaus at both little and very high CaO content. To better understand the topological origin of the composition dependence of T_g values, we calculate the contributions from each constraint on T_g , which is shown in **Figure 1. 10(b)**. The analysis yields expected results, as both Si BB and BB constraints contributing to the network are active throughout the whole composition range due to the fact that they are rigid constraints. As CaO content increases, more Ca-NBO BS constraints become active, while portions of constraints associated with Si start to break. At the same time, the Si-BO-Si BB constraints start to contribute to the system rigidity, which eventually all turn inactive at the point when all BO are consumed as Ca atoms depolymerize the network. Note that the Si-BO-Si BB constraints are not included at x = 0 due to the fact that pure silica should be viewed as an exception in terms of topology. It is for the same reason that our simulations start with $(CaO)_{10}(SiO_2)_{90}$ instead of pure silica. Also, the result aligns with the previously determined onset temperature of Si-BO-Si and O-Si-O BB constraints: T_1 = 1350 K and T_2 = 2250 K, respectively.

Our analysis suggests that for the different composition ranges, the constraints that contribute to $T_g(x)$ are different. Specifically, (i) for small x, Si BS and Ca-NBO BS constraints are intact (O-Si-O BB constraints break at T_2 = 2250 K), (ii) for moderate CaO content region, Si BS, Ca-

NBO BS and O-Si-O BB constraints are active, and (iii) for large *x*, region, Si BS, Ca-NBO BS, O-Si-O BB, and Si-BO-Si BB constraints are all active (Si-BO-Si BB constraints break at T_1 = 1350 K). However, due to the fact that BO atoms are likely all consumed at large *x*, there are no contributions from Si-BO-Si BB constraints as there would supposedly be. In addition, we believe that the high coordination number of Ca atoms compensates for the loss of rigidity due to the depolymerization of the network.

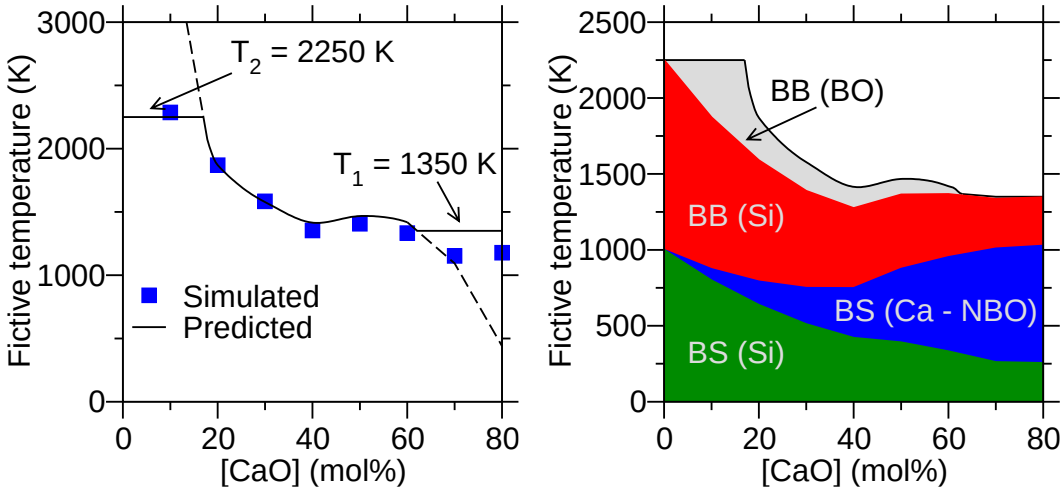

(a) (b)

Figure 1. 10 **(a)** The simulated and predicted T_f values of the $(CaO)_{50}(SiO_2)_{50}$ glass as a function of the CaO composition. **(b)** Composition dependence of predicted T_f decomposed into different contributions originated from different constraints.

We then assess the rigidity of the network for three different ranges, namely (i) $T < T_1$ (large *x* with high CaO content), (ii) $T_1 < T < T_2$ (moderate CaO content), and (iii) $T > T_2$ (small *x* with little CaO content). According to **Eq.10**, T_g is inversely proportional to the degrees of freedom per atom. Here we present the number of constraints and degrees of freedom per atom as a function of CaO composition in the three different composition ranges (**Figure 1. 11**). The

results echo the analytical model, where (i) for $T < T_1$, the number of constraints per atom is larger than 3 and the system is stressed-rigid (overconstrained), (ii) for $T_1 < T < T_2$, the number of constraints per atom is slightly below 3 and thus the system has certain flexibility, and (iii) for $T > T_2$, the network has the most degree of freedom among the three regions hence the system is flexible (underconstrained). This concept is also in accordance with the fact that constraints have their own free energy, so the more they contribute to the rigidity of the network, the higher the glass transition temperature would be. Similarly, stronger constraints have higher onset temperatures where they break and become inactive.

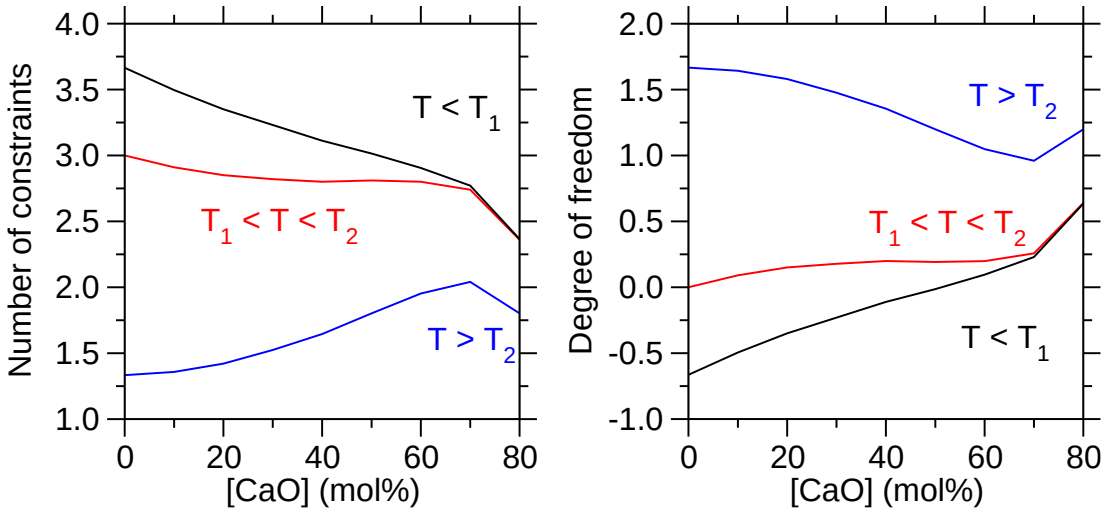

Figure 1. 11 **(a)** The number of constraints per atom and **(b)** degree of freedom per atom, respectively, as a function of [CaO] mol%. T_1 = 1350 K and T_2 = 2250 K.

1.4.5 Limitations

In general, the methodology presented above enables direct access to the topological environment of the glass network thus providing a model linking glass transition temperature with composition. However, limitations exist, among which the most noteworthy one is due to the nature of MD simulation. Because of the high cooling rate used in MD, simulated glasses often show higher fictive temperatures than those measured experimentally[50,51]. As a result, the onset temperatures may be overestimated here. If one were to use them for real glass applications, rescaling would be necessary. It has been shown that by extrapolating MD simulation results that are performed at different cooling rates (i.e., from 100 to 0.001K/ps), one can access results that are close to those from experimental cooling rates (i.e., around 1K/s)[27,52] .

The other limitation comes from TCT, which is due to the fact that the number of BS constraints of a specific atom does not necessarily match its geometric coordination number. For example, Na atoms usually have 6 nearest neighbors within their first coordination shell, however, they typically have only one single BS constraint in the framework of TCT[38].

In addition, the angular excursion methodology does not always successfully take into account mutually-redundant constraints. To give an example, consider a set of three atoms: 1, 2 and 3. According to our methodology, there exist 2 BS constraints (1-2 and 2-3) and 1 BB constraint (angle 123). Nevertheless, when calculating angular excursion, the relative motion between atoms 1 and 3 may be low. Even though there is no such 1-3 BS constraint, the interatomic environment of atom 1 and 3 is still captured anyways. This is the result of the fact that the

triangular structure of 1, 2 and 3 is already fully defined by the distance between 1-2 and 2-3 together with the 123 angle. Consequently, 1-3 distance would be redundant. Thanks to the relatively large angular excursions observed in glass systems, this limitation is less encountered[53,54].

1.5 Conclusions

By performing MD simulations, we are able to develop a topological model for the $(CaO)_x(SiO_2)_{1-x}$ glass system that predicts the fictive T_g with the input of composition only. The behavior of the model well-matches the results calculated directly from simulations. The trend of T_g can attribute to the contribution of four temperature-dependent constraints: Si BS, Ca-NBO BS, O-Si-O BB, and Si-BO-Si BB constraints. Due to the limitations inherently carried by MD simulations, further efforts could be focused on extrapolating and rescaling the results to meet those from experimental cooling rates. In addition, whether the methodologies used here would work for other glass systems still remains to be substantiated by future works.

1.6 Acknowledgments

The work presented in this chapter is in preparation for publication. It is co-authored by Zegao Liu, Kai Yang, N. M. Anoop Krishnan, Morten M. Smedskjaer and Mathieu Bauchy. The research is directed by Mathieu Bauchy.

The authors acknowledge some financial support for this research provided by the National Science Foundation under Grants No. 1762292, 1826420, and 1928538, as well as the International Cooperation on Scientific and Technological Innovation Programs of BGRIMM under Grant No. 2017YFE0107000.

1.7 References

1. Stixrude, L. & Karki, B. Structure and Freezing of MgSiO3 Liquid in Earth's Lower Mantle. *Science* **310**, 297–299 (2005).
2. Mysen, B. O., Virgo, D. & Seifert, F. A. The structure of silicate melts: Implications for chemical and physical properties of natural magma. *Rev. Geophys.* **20**, 353 (1982).
3. Bouhadja, M., Jakse, N. & Pasturel, A. Structural and dynamic properties of calcium aluminosilicate melts: A molecular dynamics study. *The Journal of Chemical Physics* **138**, 224510 (2013).
4. López-Noriega, A. *et al.* Ordered Mesoporous Bioactive Glasses for Bone Tissue Regeneration. *Chem. Mater.* **18**, 3137–3144 (2006).
5. Zhou, Q., Wang, M., Guo, L., Boolchand, P. & Bauchy, M. Intermediate Phase in Calcium–Silicate–Hydrates: Mechanical, Structural, Rigidity, and Stress Signatures. *Front. Mater.* **6**, 157 (2019).
6. Mysen, B. Physics and chemistry of silicate glasses and melts. *ejm* **15**, 781–802 (2003).
7. Zheng, Q. & Mauro, J. C. Viscosity of glass-forming systems. *J. Am. Ceram. Soc.* **100**, 6–25 (2017).
8. Mauro, J. C., Yue, Y., Ellison, A. J., Gupta, P. K. & Allan, D. C. Viscosity of glass-forming liquids. *Proceedings of the National Academy of Sciences* **106**, 19780–19784 (2009).
9. Lee, K.-H. *et al.* Topological model for Bi2O3-NaPO3 glasses. I. Prediction of glass transition temperature and fragility. *Journal of Non-Crystalline Solids* **521**, 119534 (2019).
10. Phillips, J. C. Topology of covalent non-crystalline solids I: Short-range order in chalcogenide alloys. *Journal of Non-Crystalline Solids* **34**, 153–181 (1979).

11. Thorpe, M. F. Continuous deformations in random networks. *Journal of Non-Crystalline Solids* **57**, 355–370 (1983).
12. Phillips, J. C. & Thorpe, M. F. Constraint theory, vector percolation and glass formation. *Solid State Communications* **53**, 699–702 (1985).
13. Cai, Y. & Thorpe, M. F. Floppy modes in network glasses. *Phys. Rev. B* **40**, 10535–10542 (1989).
14. Gupta, P. K. & Mauro, J. C. Composition dependence of glass transition temperature and fragility. I. A topological model incorporating temperature-dependent constraints. *The Journal of Chemical Physics* **130**, 094503 (2009).
15. Mauro, J. C., Gupta, P. K. & Loucks, R. J. Composition dependence of glass transition temperature and fragility. II. A topological model of alkali borate liquids. *The Journal of Chemical Physics* **130**, 234503 (2009).
16. Kaseman, D. C., Retsinas, A., Kalampounias, A. G., Papatheodorou, G. N. & Sen, S. Q-Speciation and Network Structure Evolution in Invert Calcium Silicate Glasses. *J. Phys. Chem. B* **119**, 8440–8445 (2015).
17. Eriksson, G. & Pelton, A. D. Critical Evaluation and Optimization of the Thermodynamic Properties and Phase Diagrams of the CaO-AI2Oa, AI203-SiO2, and CaO-AI203-SiO2 Systems. *METALLURGICAL TRANSACTIONS B* 10.
18. Maxwell, J. C. L. *On the calculation of the equilibrium and stiffness of frames*. *The London, Edinburgh, and Dublin Philosophical Magazine and Journal of Science* **27**, 294–299 (1864).
19. Boolchand, P. *et al.* Lamb-Mössbauer factors as a local probe of floppy modes in network glasses. *Journal of Non-Crystalline Solids* **182**, 143–154 (1995).

20. Chen, P. *et al.* Intermediate phase, network demixing, boson and floppy modes, and compositional trends in glass transition temperatures of binary $\textAs_x\textS_1\ensuremath-x$ system. *Phys. Rev. B* **78**, 224208 (2008).
21. Micoulaut *, M., Malki, M., Simon, P. & Canizares, A. On the rigid to floppy transitions in calcium silicate glasses from Raman scattering and cluster constraint analysis. *Philosophical Magazine* **85**, 3357–3378 (2005).
22. Novita, D. I., Boolchand, P., Malki, M. & Micoulaut, M. Elastic flexibility, fast-ion conduction, boson and floppy modes in $AgPO_3$–AgI glasses. *J. Phys.: Condens. Matter* **21**, 205106 (2009).
23. Wang, F., Mamedov, S., Boolchand, P., Goodman, B. & Chandrasekhar, M. Pressure Raman effects and internal stress in network glasses. *Phys. Rev. B* **71**, 174201 (2005).
24. Adam, G. & Gibbs, J. H. On the temperature dependence of cooperative relaxation properties in glass-forming liquids. *Journal of Chemical Physics* **43**, 139 (1965).
25. Naumis, G. G. Energy landscape and rigidity. *Phys. Rev. E* **71**, 026114 (2005).
26. Naumis, G. G. Glass transition phenomenology and flexibility: An approach using the energy landscape formalism. *Journal of Non-Crystalline Solids* **352**, 4865–4870 (2006).
27. Li, X. *et al.* Cooling rate effects in sodium silicate glasses: Bridging the gap between molecular dynamics simulations and experiments. *The Journal of Chemical Physics* **147**, 074501 (2017).
28. Cormack, A. N., Du, J. & Zeitler, T. R. Alkali ion migration mechanisms in silicate glasses probed by molecular dynamics simulations. *Phys. Chem. Chem. Phys.* **4**, 3193–3197 (2002).

29. Bauchy, M. & Micoulaut, M. From pockets to channels: Density-controlled diffusion in sodium silicates. *Phys. Rev. B* **83**, 184118 (2011).
30. Krishnan, N. M. A. *et al.* Enthalpy Landscape Dictates the Irradiation-Induced Disordering of Quartz. *Phys. Rev. X* **7**, 031019 (2017).
31. Wang, B., Yu, Y., Pignatelli, I., Sant, G. & Bauchy, M. Nature of radiation-induced defects in quartz. *J. Chem. Phys.* **143**, 024505 (2015).
32. Nosé, S. A molecular dynamics method for simulations in the canonical ensemble. *Molecular Physics* **52**, 255–268 (1984).
33. Hoover, W. G. Canonical dynamics: Equilibrium phase-space distributions. *Phys. Rev. A* **31**, 1695–1697 (1985).
34. Du, J. & Cormack, A. N. The medium range structure of sodium silicate glasses: a molecular dynamics simulation. *Journal of Non-Crystalline Solids* **349**, 66–79 (2004).
35. Bauchy, M. Structural, vibrational, and elastic properties of a calcium aluminosilicate glass from molecular dynamics simulations: The role of the potential. *The Journal of Chemical Physics* **141**, 024507 (2014).
36. Plimpton, S. J. Fast Parallel Algorithms for Short-range Molecular Dynamics. *Journal of Computational Physics* 1–19 (1995).
37. Micoulaut, M., Raty, J.-Y., Otjacques, C. & Bichara, C. Understanding amorphous phase-change materials from the viewpoint of Maxwell rigidity. *Phys. Rev. B* **81**, 174206 (2010).
38. Bauchy, M. & Micoulaut, M. Atomic scale foundation of temperature-dependent bonding constraints in network glasses and liquids. *Journal of Non-Crystalline Solids* **357**, 2530–2537 (2011).

39. Bauchy, M. *et al.* Angular rigidity in tetrahedral network glasses with changing composition. *Phys. Rev. B* **84**, 054201 (2011).

40. Bauchy, M. & Micoulaut, M. Transport Anomalies and Adaptative Pressure-Dependent Topological Constraints in Tetrahedral Liquids: Evidence for a Reversibility Window Analogue. *Phys. Rev. Lett.* **110**, 095501 (2013).

41. Bauchy, M. Topological Constraints and Rigidity of Network Glasses from Molecular Dynamics Simulations. *arXiv:1506.06483 [cond-mat]* (2015).

42. Bauchy, M., Micoulaut, M., Boero, M. & Massobrio, C. Compositional Thresholds and Anomalies in Connection with Stiffness Transitions in Network Glasses. *Phys. Rev. Lett.* **110**, 165501 (2013).

43. Micoulaut, M. & Bauchy, M. Anomalies of the first sharp diffraction peak in network glasses: Evidence for correlations with dynamic and rigidity properties. *Phys. Status Solidi B* **250**, 976–982 (2013).

44. Bauchy, M. & Micoulaut, M. Densified network glasses and liquids with thermodynamically reversible and structurally adaptive behaviour. *Nat Commun* **6**, 6398 (2015).

45. Bauchy, M., Abdolhosseini Qomi, M. J., Bichara, C., Ulm, F.-J. & Pellenq, R. J.-M. Nanoscale Structure of Cement: Viewpoint of Rigidity Theory. *J. Phys. Chem. C* **118**, 12485–12493 (2014).

46. Bauchy, M. *et al.* Fracture toughness anomalies: Viewpoint of topological constraint theory. *Acta Materialia* **121**, 234–239 (2016).

47. Qomi, M. J. A., Bauchy, M., Ulm, F.-J. & Pellenq, R. J.-M. Anomalous composition-dependent dynamics of nanoconfined water in the interlayer of disordered calcium-silicates. *The Journal of Chemical Physics* **140**, 054515 (2014).
48. Lindemann, F. A. The calculation of molecular Eigen-frequencies. (1984).
49. Smedskjaer, M. M., Mauro, J. C., Sen, S. & Yue, Y. Quantitative Design of Glassy Materials Using Temperature-Dependent Constraint Theory. *Chem. Mater.* **22**, 5358–5365 (2010).
50. Du, J. Challenges in Molecular Dynamics Simulations of Multicomponent Oxide Glasses. in *Molecular Dynamics Simulations of Disordered Materials: From Network Glasses to Phase-Change Memory Alloys* (eds. Massobrio, C., Du, J., Bernasconi, M. & Salmon, P. S.) 157–180 (Springer International Publishing, 2015). doi:10.1007/978-3-319-15675-0_7.
51. Huang, L. & Kieffer, J. Challenges in Modeling Mixed Ionic-Covalent Glass Formers. in *Molecular Dynamics Simulations of Disordered Materials* (eds. Massobrio, C., Du, J., Bernasconi, M. & Salmon, P. S.) vol. 215 87–112 (Springer International Publishing, 2015).
52. Bhaskar, P. *et al.* Cooling rate effects on the structure of 45S5 bioglass: Insights from experiments and simulations. *Journal of Non-Crystalline Solids* **534**, 119952 (2020).
53. Wang, M. *et al.* Crucial effect of angular flexibility on the fracture toughness and nano-ductility of aluminosilicate glasses. *Journal of Non-Crystalline Solids* **454**, 46–51 (2016).
54. Zhang, M. & Boolchand, P. The Central Role of Broken Bond-Bending Constraints in Promoting Glass Formation in the Oxides. *Science* **266**, 1355–1357 (1994).

Chapter 2 Topological Origin of Glass-forming Ability in Calcium Silicates

2.1 Introduction

It is known that a material can be made glassy or amorphous if it is cooled from its liquid state fast enough, even if this material is crystalline. However, in order to be "fast enough", some materials have easily accessible critical cooling rates, while others may require extremely high rates. The extent of difficulty in achieving this critical cooling rate is generally believed to be a metric characterizing the glass-forming ability of this material[1]. Nevertheless, the physical mechanism behind this has remained not fully understood.

Zachariasen, known as the founding father of glass science, put forward four rules of glass formation in his famous 1932 paper[2]. His work established a cornerstone for glass pioneers who later on analyzed and improved the glass forming-ability theory based on his empirical insight of both short-range and long-range order of macroscopic disorder network. Following Zachariasen, Phillips further developed the concept of constraint calculation in his 1979 paper[3] for chalcogenides, proposing a model for glass-forming ability as a function of composition. This served as a mathematical prototype for the topological constraint theory (TCT) which came out later by him and Thorpe. Later in 1990, Gupta and Cooper[4] set a mathematical foundation for Zachariasen's first two rules, deriving the existence of infinitely large, *d*-dimensional and topologically disordered networks. Their work generalized the Zachariasen's criteria to

unrestricted dimensional space. To be specific, the polyhedra units in the original three-dimensional case are extended to polytope units of arbitrary dimensionality[5]. Based on the result of this collaboration, Gupta added a hint of topological viewpoint to the glass-forming ability theory in his own work later[1]. Considering rigidity and connectivity in the network, he demonstrated mathematically by calculating degrees of freedom per vertex, *f*, that a network "neither too connected, nor too flexible" corresponds to high glass-forming ability.

On the other hand, experimental results also gave us a glimpse into the origin of glass-forming ability. Specifically for CS glasses, within a $(CaO)_x(SiO_2)_{1-x}$ network , x = 42 – 61% was demonstrated to be the range having the best glass-forming ability by Eriksson and Pelton[6]. According to their work, large mole fraction of CaO could cause phase separations, whereas lower mole fraction of CaO led to a liquidous that was extremely high for glass to form. Hence the compositional window in-between was observed to have the highest glass-forming ability.

All these theories provided solid insights into the nature of glass-forming ability, however, more details from a physical aspect, for instance, internal stress, mean-squared displacement of the atoms, connectivity, etc., would assist in explaining the long eluded reason why the empirical theories worked. The goal here is to decipher the glass-forming ability from the aspects of both topological and physical details, focusing on calcium silicate glasses. For simplicity, we perform MD simulations of a series of CS glasses using a 3D bond-bending model, which allows us to consider networks that are practical in real-life applications. We then analyze the properties of the networks, including coordination numbers, constraints calculation, mean-squared

displacements and stress calculation, etc. According to the topological constraint theory, we find that the optimal glass-forming ability occurs at [CaO] mol% = 50%, which is in accordance with previous attempts to analyze phase transitions in CS systems[6]. Our results of structural details and internal stress help explain this critical composition, as it coincides with both rigidity and stress transition within the network.

2.2 Results and Discussion

2.2.1 Structure

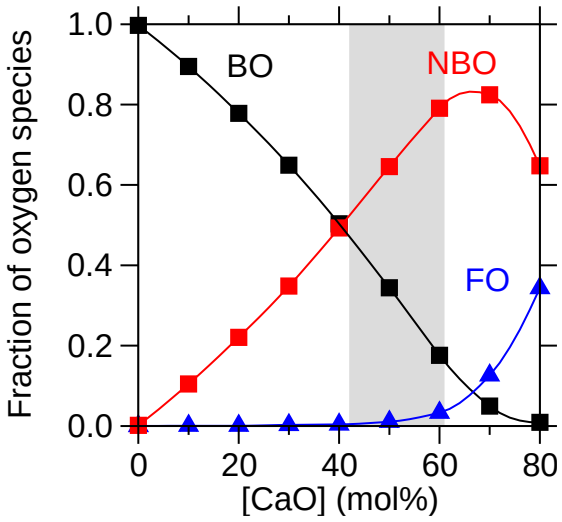

Figure 2. 1 Fractions of different types of oxygen atoms as a function of [CaO] mol%. BO: bridging oxygen, which connects two Si atoms; NBO: non-bridging oxygen, which connects one Si atom and one Ca atom; FO: free oxygen, connected with and only with at least two Ca atoms. The solid lines serve as a guide to the eye. The grey area corresponds to the compositional window where CS system demonstrates the best glass-forming ability[6].

We first focus on the identification of the atomic structures within the CS glasses simulated. As shown in **Figure 2. 1**, as more CaO content is added to the system, the number of BO decreases and the number of NBO increases. This is expected according to our analytical model (see Section 4: Methodology), since theoretically, each Ca atom added to the system would create two NBO. However, what is not predicted in the analytical model is the formation of FO, which dramatically increases starting at [CaO] mol% = 70 %. The formation of FO is due to the fact that an added Ca atom does not necessarily consume a BO first. Instead, it can possibly connect to an NBO, thus creating an FO. This has a larger possibility to happen when the concentration of CaO is relatively higher or when the system is almost saturated with glass modifier, where there are much more NBO than BO.

We then look at the Ca coordination number and the contributions coming from different oxygen species to further access the structural details of the glasses. **Figure 2. 2** presents the average Ca coordination number together with the contributions. The coordination number that comes from all oxygen species in total has a steady distribution and is always around 6, which yields expected result as it is the usual coordination number of Ca in a crystal lattice. On the other hand, the contributions coming from BO, NBO and FO all share the same trend as that of the fraction of different species in **Figure 2. 1**. Both analyses yield expected structural details, which show the validity of applying TCT in this glass system and lay a sound foundation for constraints enumeration and evaluations of the glass-forming ability of the system.

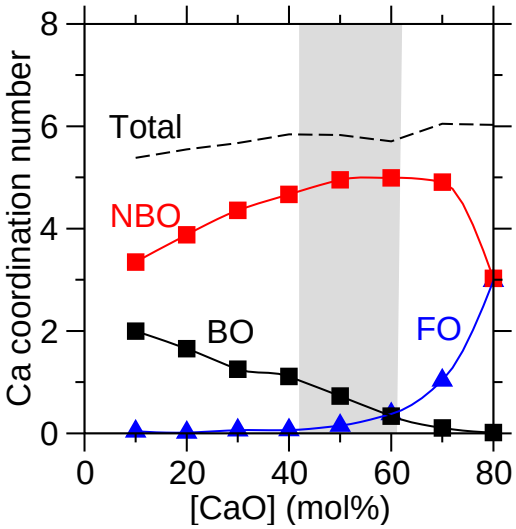

Figure 2. 2 The average coordination number of all Ca atoms as a function of [CaO] mol%. The contribution of BO, NBO, and FO are also demonstrated, which is in accordance with the observation in Figure 1. The lines serve as a guide to the eye. The grey area corresponds to the compositional window where CS system demonstrates the best glass-forming ability[6].

2.2.2 Topological Constraints Enumeration

In order to analyze the structural properties of the simulated glasses, we adopt the framework of topological constraints theory (TCT) to evaluate the rigidity of the network. TCT has the advantage of eliminating the complicated atomic networks of glasses and filtering out the chemical details that eventually do not have a critical impact on macroscopic properties, thus helps us access the structural information with a simple calculation of mechanical trusses of the network[5]. The main concepts and detailed enumeration methodology are elaborated in **Section 2.4.2**.

In **Figure 2. 3**, we calculate the number of BB and BS constraints per atom, respectively, as a function of composition. By counting all BB/BS constraints within the glass network at a certain composition, we are able to divide that by the total number of atoms (around 3000 for all compositions). These normalized values provide a general view of the rigidity condition of the network. The number of BB constraints per atom is larger than that of BS constraints per atom at first, and after [CaO] mol% exceeds around 35 %, BS constraints gradually dominate as more Ca atoms depolymerize the glasses. The sudden drop for BS constraints comes from the formation of FO which is demonstrated in **Figure 2. 2**. We note that the grey area, corresponding to the composition window where CS glasses have the best glass-forming ability[6], is when BS constraints start to outnumber BB constraints.

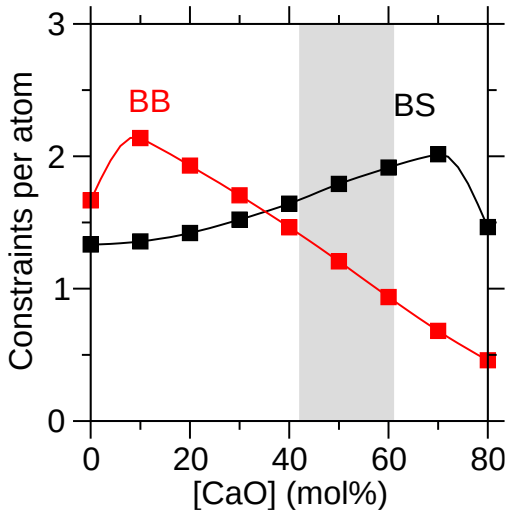

Figure 2. 3 The constraints per atom as a function of [CaO] mol%. BB: bond-bending angular constraint; BS: bond-stretching radial constraint. The solid lines serve as a guide to the eye. The grey area corresponds to the compositional window where CS system demonstrates the best glass-forming ability[6].

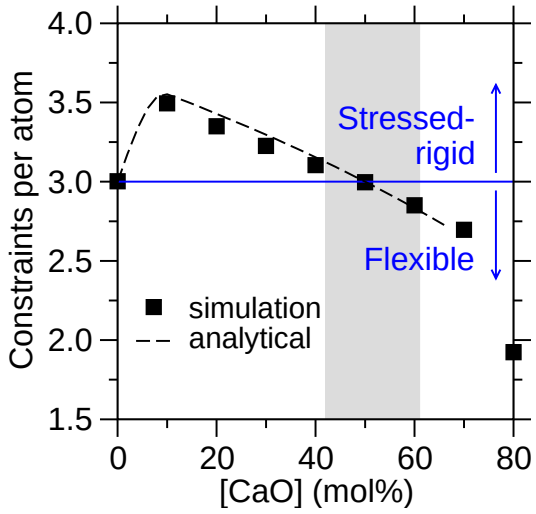

Figure 2. 4 Number of all constraints per atom (nc) as a function of [CaO] mol% composition. The black dashed line is the analytical model, and the black squares show the simulation results. The grey area corresponds to the compositional window where CS system demonstrates the best glass-forming ability[6].

The total constraints per atom is plotted in **Figure 2. 4** as a function of CaO content, where the analytical model is compared with the simulated results. The analytical model terminates at x = 0.67, n_c = 2.71, where all the BOs are consumed. As demonstrated in **Figure 2. 2**, the contribution of BS constraints around Ca atoms is also utilized to fill in the gap during calculation. The blue line represents the isostatic threshold, where n_c = 3. When n_c > 3, the system is stressed-rigid; when n_c < 3, the system is flexible, as indicated by the blue arrows. The rigidity of CS glasses decreases as more CaO is added to the system, since Ca atoms depolymerize the network due to the formation of NBO (non-bridging oxygen atoms). According to the analytical model, CS system has its flexible-to-rigid transition at x_{iso} = 50%, which agrees again with where the glass-forming ability is observed to be optimal empirically.

2.2.3 Origin of Glass-forming Ability

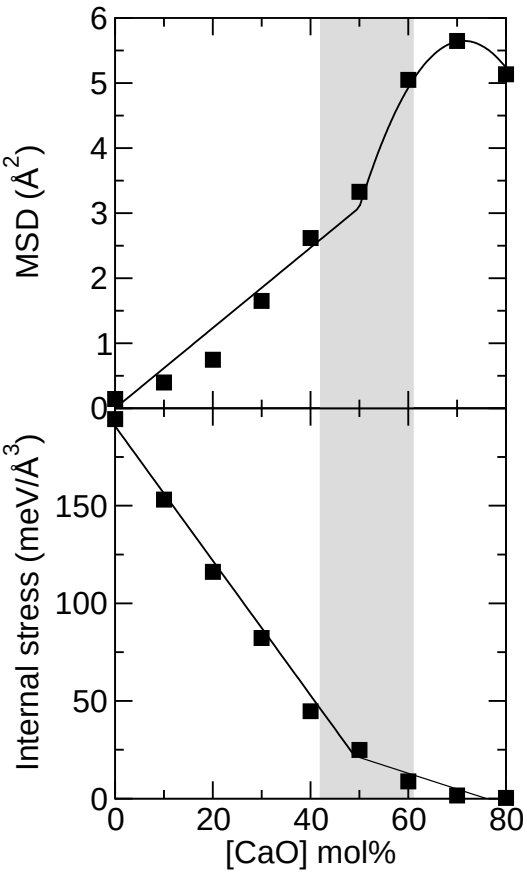

Figure 2. 5 **(a)** mean squared displacement (MSD) of all atoms and **(b)** internal stress per BO as a function of [CaO] mol%. The solid lines serve as a guide to the eye. The grey area corresponds to the compositional window where CS system demonstrates the best glass-forming ability[6].

After analyzing the MD results utilizing the TCT, we now focus on understanding this window of best glass-forming ability from the aspect of physical details, namely internal flexibility and the internal stress per BO of the calcium silicate network.

To assess the internal flexibility of the glasses, we refer to the extent of atomic mobility of the system following an external stimulus[7–9]. The methodology of mean squared displacement

(MSD) measurements is elaborated in **Section 2.4.3** and thus presented in **Figure 2. 5 (a)**. Note that MSD increases when [CaO] mol% increases, and it shows a break of slope at [CAO] mol% = 50%, which again corresponds to the composition that has the optimal glass-forming ability and indicates the existence of the flexible-to-rigid transition. The physical explanation behind this methodology is that, a larger MSD indicates higher atomic mobility, thus flexible glasses ($n_c < 3$) demonstrate a noticeable larger value of MSD. As in flexible glasses, relaxation is "kinetically-favored" due to the fact that atoms have high mobility, the system can thus relax toward its lower-energy configurations. On the other hand, stressed-rigid glasses ($n_c > 3$, [CaO] mol% < 50%) have lower MSD, but there exists more internal stress in the network.

To further investigate the origin of the glass-forming ability, we evaluate the internal stress within the network. Since NBO and FO are disconnected from the backbone structure, we focus on the internal stress of BO. **Figure 2. 5 (b)** shows the internal stress per BO as a function of the glass composition, which is the difference between the reference stress and the stress in bulk glasses. With the detailed calculation listed in **Section 2.4.4**, this internal topological network stress comes from the various constraints in the atomic network that mutually depend on each other. In general, the internal stress monotonically decreases with the increase of [CaO] mol%. Again, there exists a break in slope at 50 % of CaO, which indicates the flexible-to-stressed transition.

2.3 Conclusions

By conducting MD simulations and analyzing results, we are able to approach an accurate description of the structural topology and rigidity of calcium silicate glasses. The topological constraint theory confirms a flexible-to-rigid transition (i.e., flexible and rigid at high and low CaO content, respectively), which is in accordance with the empirical result of the compositional window that shows optimal glass-forming ability. We know that this transition comes from the competition between internal atomic mobility and internal stress, providing a glimpse into the origin of glass-forming ability. Note that the methodologies used (i.e., TCT analytical model, MSD and internal stress, etc.) combined with MD simulations can ultimately be applied to many other glass systems and study various properties. For future work, they can also help develop fully analytical models that can predict glass properties as a function of composition, which is promising to accelerate the design of novel glass applications.

2.4 Methodologies

2.4.1 Preparation of the Melts

We first simulate a series of calcium silicate glasses $(CaO)_x(SiO_2)_{1-x}$ within the range of x = 0 ~ 80% by molecular dynamics. The potential used to simulate the CS glasses was developed by Jakse *et al*[10]. This interatomic potential relies on fixed partial charges and a simple two-body Buckingham potential formulation. A timestep of 1 fs is used and the Coulombic interactions are evaluated with the Ewald summation method, with a convergence criterion factor of 10^{-5}[5, 9,11–16]. For the short-range and Coulombic interactions, the cutoffs are 8 and 12 Å[17], respectively. This potential was demonstrated to provide a sound description of the structural and elasticity

properties of CS glasses[18]. When preparing the melts using LAMMPS package[19], the initial liquid configurations are generated by randomly allocating around 3000 atoms in a cubic simulation box, while at the same time avoiding any unrealistic overlap. Then the system is equilibrated at 3000 K for 100 ps in *NVT* ensemble to ensure the loss of the memory of the initial configurations. Following that, the system is relaxed at 3000 K in *NPT* ensemble (under zero pressure) for another 100 ps. Then the glass is ready to be cooled at the rate of 1 K/ps from 3000 K to room temperature, 300 K, with the cooling increment of 100 K during temperature decrease. Finally, the system is subjected to a final relaxation by staying at room temperature for 100 ps.

2.4.2 Topological Constraints Enumeration

There are two types of mechanical constraints that the atoms within the system undergo from chemical interactions: the 2-body radial bond-stretching (BS) constraints and the 3-body angular bond-bending (BB) constraints. According to Maxwell's criterion of stability for mechanical trusses[20,21], glassy networks can either be flexible, stressed-rigid, or isostatic, when the number of constraints per atom (n_c) is lower, higher, or equal, respectively, to 3.

The analytical model is based on several basic assumptions. Firstly, the fraction of each element is calculated based on the hypothesis that each Ca atom creates two NBO atoms. Since the fraction of Ca, Si and O atoms are known according to $(CaO)_x(SiO_2)_{1-x}$, we can simply assume the fraction of NBO is twice the fraction of Ca atoms. Based on that, we further assume that there are only two types of O atoms, BO and NBO (no FO), which supports the formula: BO = O – NBO. Secondly, when establishing the coordination number (CN) of each element, for Ca

atoms, it is assumed that their local environment of oxygen atoms would always obey CN_Ca-O = 5. Note that we assume there is no BB constraint of Ca atoms, given that their angular configuration is not clearly defined. On the other hand, for Si atoms, it is agreed that the Si tetrahedra are very stable, hence CN_Si-O = 4. Thirdly, in general, all BS constraints are fully attributed to cations, i.e. Ca and Si atoms, while there is no limitation applied to BB constraints. The number of BS constraints is determined according to *r*, the CN of each element, while the number of BB constraints complies with the following formula[5]: $n_{BB} = 2r - 3$.

With that said, the calculation of the n_c of the simulated glasses is demonstrated in **Table 1** and the resulting analytical model of n_c is the following equation:

$$n_c = \frac{11 - 7x}{3 - x} \quad \text{Eq. 166}$$

Note that the analytical model terminates at $x = 0.67$, $n_c = 2.71$, where all BOs are consumed by the added Ca atoms, and the assumptions no longer hold true.

Both the analytical model and simulation results of constraints per atom are shown and compared in **Figure 2. 4**.

Table 1. Analytical calculation of constraints per atom.

	fraction	CN	BS	BB	BS+BB
Ca	x	5	5	0	5
O	2-x	\	\	\	\
BO	2-3x	2	\	1	1
NBO	2x	1	\	0	0
Si	1-x	4	4	5	9

2.4.3 Mean Squared Displacement

To study the effect in atomic mobility, we first prepare a series of CS glass configurations corresponding to the previous chemical compositions. Note that the configurations are chosen to be relaxed at 0 K, so they are made sure to reach their local minimum within the energy landscape without the memory of their inherent configuration. Then, we impose an instantaneous energy bump of 3000 K (258.6 meV/Å3), which is achieved by manually attributing kinetic energy to the atoms9. The response of the system is then recorded and calculated for 200 ps in NVE ensemble. Since this external kinetic energy is equipartitioned, half of it is consumed in temperature increase, while the other half contributes to the potential energy of the system through atomic displacement. The energy bump is chosen so that the temperature remains relatively low compared with the fictive temperature of the glasses, so that they would not melt. Then the final mean-squared displacement (MSD) of the atoms after the energy bump is recorded to evaluate the extent of atomic mobility. With 200 ps being long enough to observe a plateau in

MSD, this value provides an insight into the local curvature of the enthalpy landscape. System exhibiting a rough enthalpy landscape with some well-defined energy basins tends to show low MSD values, whereas system exhibiting smooth enthalpy landscape is more likely to generate high MSD values, due to the fact that it is easier for atoms to overcome smaller energy barriers.

2.4.4 Stress Calculation

For stress calculation, we utilize the "stress per atom" framework developed by Thompson *et al*[22]. According to their theory, the following formula defines the stress (σ_i) of each atom (i) as the individual contribution of each atom to the system:

$$3\sigma_i V_i = m_i v_i^2 + \overrightarrow{r_k} \cdot \overrightarrow{F_k} \qquad \text{Eq. 17}$$

Where V_i, m_i, v_i, and $\overrightarrow{r_k}$ are the volume, mass, velocity, and position of the atom i, and $\overrightarrow{F_k}$ is the resultant force applied on atom i by all other atoms in the system.

Here, we focus on the stress of bridging-oxygen (BO) atoms. There are several concepts that need to be introduced. Firstly, we define reference stress as a localized stress that would be undergone by an atom inside a cluster. This comes from the observation that even an isolated SiO_4 unit has some stress within itself due to a competition between Si-O attraction and O-O repulsion[23,24]. With that said, we define bulk stress as the average stress of the glass system calculated directly from MD simulations. Based on that, we can finally define internal stress as the result of bulk stress subtracting the reference stress.

To calculate the reference stress, we first simulate a Q4-Q4 cluster. The initial configuration is generated by allocating 39 atoms in a cubic simulation box with the side length of 20 Å, including 8 Si atoms, 25 O atoms and 9 Ca atoms, without periodic boundary conditions. Each Q4 structure has 4 Si tetrahedra and is connected by three BO atoms. The position of each atom is allocated based on the average values of their bond lengths and inter-atomic angles[25]. The system is then equilibrated at 300 K for 100 ps, followed by being cooled from 300 K to 0 K with a cooling rate of 1 K/ps, both in *NVT* ensemble. During this process, the linear and angular momentum of the cluster are also fixed to zero to avoid any instability of the system, followed with a final energy minimization. After that, the average stress undergone by all BOs is evaluated, which is defined as the bulk stress. 99999cx Following that, the reference stress is quantified by subtracting the Q4-Q4 reference stress from the average stress of BOs in the glasses calculated by LAMMPS. By multiplying BO eigenstress with the number of BOs, and then dividing it by the number of all atoms in the glass, we calculate the eigenstress of all BOs normalized by the number of atoms. Lastly, the unit is converted to meV/Å^3.

2.5 Acknowledgments

The work presented in this chapter is in preparation for publication. It is co-authored by Zegao Liu, N. M. Anoop Krishnan, Christian G. Hoover, Morten M. Smedskjaer and Mathieu Bauchy. The research is directed by Mathieu Bauchy.

The authors acknowledge some financial support for this research provided by the National Science Foundation under Grants No. 1762292, 1826420, and 1928538, as well as the International Cooperation on Scientific and Technological Innovation Programs of BGRIMM under Grant No. 2017YFE0107000.

2.6 References

1. Gupta, P. K. Rigidity, Connectivity, and Glass-Forming Ability. *J American Ceramic Society* **76**, 1088–1095 (1993).
2. Zachariasen, W. H. THE ATOMIC ARRANGEMENT IN GLASS. *J. Am. Chem. Soc.* **54**, 3841–3851 (1932).
3. Phillips, J. C. Topology of covalent non-crystalline solids I: Short-range order in chalcogenide alloys. *Journal of Non-Crystalline Solids* **34**, 153–181 (1979).
4. Gupta, P. K. & Cooper, A. R. Topologically disordered networks of rigid polytopes. *Journal of Non-Crystalline Solids* **123**, 14–21 (1990).
5. Mauro, J. C. Topological constraint theory of glass. *American Ceramic Society Bulletin* **90**, 7.
6. Eriksson, G. & Pelton, A. D. Critical Evaluation and Optimization of the Thermodynamic Properties and Phase Diagrams of the CaO-AI2Oa, AI203-SiO2, and CaO-AI203-SiO2 Systems. *METALLURGICAL TRANSACTIONS B* 10.
7. Wang, B. *et al.* Irradiation-induced topological transition in SiO2: Structural signature of networks' rigidity. *Journal of Non-Crystalline Solids* **463**, 25–30 (2017).
8. Zhou, Q., Wang, M., Guo, L., Boolchand, P. & Bauchy, M. Intermediate Phase in Calcium–Silicate–Hydrates: Mechanical, Structural, Rigidity, and Stress Signatures. *Front. Mater.* **6**, 157 (2019).
9. Krishnan, N. M. A. *et al.* Enthalpy Landscape Dictates the Irradiation-Induced Disordering of Quartz. *Phys. Rev. X* **7**, 031019 (2017).

10. Bouhadja, M., Jakse, N. & Pasturel, A. Structural and dynamic properties of calcium aluminosilicate melts: A molecular dynamics study. *The Journal of Chemical Physics* **138**, 224510 (2013).
11. Li, X. *et al.* Cooling rate effects in sodium silicate glasses: Bridging the gap between molecular dynamics simulations and experiments. *The Journal of Chemical Physics* **147**, 074501 (2017).
12. Cormack, A. N., Du, J. & Zeitler, T. R. Alkali ion migration mechanisms in silicate glasses probed by molecular dynamics simulations. *Phys. Chem. Chem. Phys.* **4**, 3193–3197 (2002).
13. Bauchy, M. & Micoulaut, M. From pockets to channels: Density-controlled diffusion in sodium silicates. *Phys. Rev. B* **83**, 184118 (2011).
14. Wang, B., Yu, Y., Pignatelli, I., Sant, G. & Bauchy, M. Nature of radiation-induced defects in quartz. *J. Chem. Phys.* **143**, 024505 (2015).
15. Nosé, S. A molecular dynamics method for simulations in the canonical ensemble. *Molecular Physics* **52**, 255–268 (1984).
16. Hoover, W. G. Canonical dynamics: Equilibrium phase-space distributions. *Phys. Rev. A* **31**, 1695–1697 (1985).
17. Du, J. & Cormack, A. N. The medium range structure of sodium silicate glasses: a molecular dynamics simulation. *Journal of Non-Crystalline Solids* **349**, 66–79 (2004).
18. Bauchy, M. Structural, vibrational, and elastic properties of a calcium aluminosilicate glass from molecular dynamics simulations: The role of the potential. *The Journal of Chemical Physics* **141**, 024507 (2014).

19. Plimpton, S. J. Fast Parallel Algorithms for Short-range Molecular Dynamics. *Journal of Computational Physics* 1–19 (1995).
20. Lagrange, J. *Mécanique Analytique*. (1788).
21. Maxwell, J. C. L. *On the calculation of the equilibrium and stiffness of frames*. *The London, Edinburgh, and Dublin Philosophical Magazine and Journal of Science* **27**, 294–299 (1864).
22. Thompson, A. P., Plimpton, S. J. & Mattson, W. General formulation of pressure and stress tensor for arbitrary many-body interaction potentials under periodic boundary conditions. *The Journal of Chemical Physics* **131**, 154107 (2009).
23. Li, X., Song, W., Smedskjaer, M. M., Mauro, J. C. & Bauchy, M. Quantifying the internal stress in over-constrained glasses by molecular dynamics simulations. *Journal of Non-Crystalline Solids: X* **1**, 100013 (2019).
24. Liu, H., Li, Y., Fu, Z., Li, K. & Bauchy, M. Exploring the landscape of Buckingham potentials for silica by machine learning: Soft vs hard interatomic forcefields. *J. Chem. Phys.* **152**, 051101 (2020).
25. Bauchy, M. Structural, vibrational and thermal properties of densified silicates : insights from Molecular Dynamics. *The Journal of Chemical Physics* **137**, 044510 (2012).

Chapter 3 Glass Relaxation and Hysteresis of the Glass Transition by Molecular Dynamics Simulations

3.1 Acknowledgments

Chapter 3 is reprinted and adapted with permission from [(Liu, Z. *et al.* Glass relaxation and hysteresis of the glass transition by molecular dynamics simulations. *Phys. Rev. B* **98**, 104205 (2018).) as follows: Zegao Liu, Yushu Hu, Xin Li, Weiying Song, Sushmit Goyal, Matthieu Micoulaut, and Mathieu Bauchy, Glass relaxation and hysteresis of the glass transition by molecular dynamics simulations, *Physical Review B* **98**, 104205 (2018). http://dx.doi.org/10.1103/PhysRevB.98.104205]

The reprint is endorsed by the committee chair and the co-authors of the article. The authors acknowledge Zegao Liu for forming the basis of the article, and Mathieu Bauchy for directing the research.

This work was supported by the National Science Foundation under Grants No. 1562066, 1762292, and 1826420, and by Corning Incorporated through the Glass Age Scholarship.

3.2 Introduction

The crystallization of a liquid can be avoided if cooled fast enough.[1] At temperatures lower than the melting temperature, supercooled liquids are a thermodynamic metastable state.[2] With decreasing temperature, the viscosity η and the relaxation time to equilibrium τ tend to dramatically increase. At some reference temperature defined in the literature as the glass transition temperature T_g, η reaches the value 10^{12} Pa·s, which roughly corresponds to a relaxation time of 100 s.[3] At lower temperatures, the very viscous liquid exhibit all the typical macroscopic properties of a solid and these properties now depend on the waiting time before the realized measurement.[4,5] This simply signals that glasses are out-of-equilibrium materials and their properties evolve slowly with time.[6]

A conventional means to measure such effects is to rely on calorimetric methods. As the equilibration cannot proceed further upon cooling (because of the rapid increase of the relaxation time with decreasing temperature) the enthalpy curve or the volume curve deviates from the high-temperature equilibrium line at the fictive temperature T_f—this temperature T_f depending explicitly on the cooling rate.[3] As a result, the specific heat (C_p) displays an abrupt decrease across T_f, which signals that the translational and rotational degrees of freedom of the glass are now frozen.[7] However, even in the resulting glassy state, the material continues to relax toward lower enthalpies, but over timescales that exceed the laboratory timescale by several orders of magnitude.[2] Upon reheating, the behavior of the specific heat is markedly different from the cooling curve and a hysteresis can be evidenced. The extent of hysteresis depends on the heating rate, the temperature at which the glass has relaxed and the waiting time before which the

calorimetric experiment is performed.[3] This heating experiment, furthermore, leads to a heat capacity overshoot at the glass transition and this endotherm signals that relaxation has taken place due to their intrinsic out-of-equilibrium nature of the glassy state.[8] Relaxation effects are technologically important as they can cause undesirable variations in the dimensions of glassy substrates for displays application during processing, which can eventually result in some pixel misalignement.[9] In select situations and applications, one is targeting a reduced relaxation tendency that can induce a minimal hysteresis in enthalpy or molar volume. However, it is not clear which physical and chemical properties drive such "ideal" glasses. Yet, it has recently been found that such hysteresis curves are minimized when the liquid reaches a critical mechanical state with an optimal reduction of both low-frequency relaxation and bond energy minima of the potential energy landscape.[10,11]

Molecular dynamics (MD) simulations can shed some light on such phenomena by relating the thermal or energy behavior with different materials properties such as structure and mechanical properties.[12] In this respect, the relaxation of glass has been related to the effects of pressure,[10] composition,[13] coordination numbers,[14] and other factors.[15] However, a well-known shortcoming of MD simulations is their timescale, which can only extend to the μs range—so that the typical timescales associated with glassy relaxation at T_g (seconds) are out-of-reach.[16] Correspondingly, the viscosity range that can be investigated is of about tens or hundreds of Pa·s only. However, one has to keep in mind that all the salient features associated with the experimental onset of an out-of-equilibrium dynamics can be recovered from simulations—although the associated time scale is shifted with respect to experiments.[17,18] This timescale difference leads to an

overestimation of the glass fictive temperature, which is usually larger in simulations by several hundred of degrees when compared to the experimental counterpart due to much larger cooling rates (on the order of a few K/ps). Such large values of cooling rates are actually fairly compatible with those experienced experimentally in very small samples, wherein surface is large as compared to volume—so that surface energy dissipation can occur fast.[19] Numerical studies have, furthermore, revealed that the relaxation time and the viscosity can be accurately investigated from simulations and associated results compare favorably with experimental data of high temperature liquids—while being sometimes extrapolated with confidence to lower temperatures.[20] Similarly, the freezing of density-density correlations in Fourier space at low temperature can also be recovered (i.e., the β-relaxation plateau associated with the cage-like dynamics of supercooled liquids) and the behavior of heat capacities across the glass transition region as is rather well-described.[15] Having such intrinsic limitations at hand, MD simulations represent, still, a powerful technique able to substantiate the notion of glass reversibility and connect the behavior with materials properties at large.

In the present contribution, we address this issue of glass reversibility by focusing on numerical cooling/heating cycles across the glass transition. We perform MD simulations of three archetypal silicate glasses: (i) silica, SiO_2, the base system for all silicate glasses,[3] (ii) sodium silicate, $(Na_2O)_{30}(SiO_2)_{70}$, a model for all alkali silicate glasses used for ion-exchange treatments,[21,22] and (iii) calcium aluminosilicate, $(CaO)_{24}(Al_2O_3)_{24}(SiO_2)_{52}$, a model for all alkali-free display glasses used for LCD/OLED glass substrates.[9] A novel methodology combining thermal cycles and inherent configuration analysis is introduced and serves for the

characterization of the features of relaxation in relationship with glass transition reversibility. We first show that our simulations reproduce the generic features of the glass transition. Following this, we find that, for all the considered glasses, enthalpy relaxation follows a power-law dependence as a function of the cooling rate—in agreement with an earlier prediction of mode-coupling theory. This permits to determine the increase of enthalpy at 0 K due to a finite cooling rate with respect to that that would be achieved for a (fictitious) zero cooling rate. Further, we demonstrate that enthalpy and volume relaxation are decoupled from each other. Then, we perform cooling/heating cycles in order to measure the degree of relaxation visible from the extent of the induced hysteresis curve. We find that both the enthalpy relaxation and the range of temperature over which it occurs are strongly system-specific, although some general conclusions can be drawn.

3.3 Simulation Details

3.3.1 Preparation of the Melts

To establish our conclusions, three archetypal silicate glasses are simulated with MD: (i) silica (S), SiO_2, (ii) sodium silicate (NS), $(Na_2O)_{30}(SiO_2)_{70}$, and (iii) calcium aluminosilicate (CAS), $(CaO)_{24}(Al_2O_3)_{24}(SiO_2)_{52}$. All simulations were carried out with the LAMMPS package.[23] The initial liquid configurations were generated by (i) randomly placing around 3000 atoms in a cubic simulations box while ensuring the absence of any unrealistic overlap, (ii) melting the system at 4000 K for 100 ps (*NVT* ensemble) to ensure the loss of the memory of the initial configuration, and (iii) relaxing the system at 4000 K under zero pressure (*NPT* ensemble) for 100 ps. For all systems, a timestep of 1 fs is used, while temperature and pressure are imposed

via a Nosé–Hoover thermostat and barostat, using some damping parameter of 100 and 1000 fs, respectively.[24,25]

Since empirical force-fields have a limited transferability over varying configurations, a specific interatomic potential was chosen for each system. However, although each potential relies on a system-specific parametrization, they all rely on fixed partial charges and a simple two-body Buckingham potential formulation. In all cases, the Coulombic interactions were evaluated with the Ewald summation method—with a convergence criterion factor of 10^{-5}. First, the well-established potential developed by van Beest, Kramer, and van Santen (BKS) was used to simulate silica.[26] The cutoff was fixed at 5.5 and 10 Å for the short-range and Coulombic interactions, respectively—as this specific choice has shown to yield an improved description of the glass density.[27] The BKS potential has shown to offer a very good description of the structural, dynamical, and mechanical properties of silica.[27–30] Second, we relied on the potential parameterized by Teter to simulate the NS glass.[31] The cutoff was fixed at 8 and 12 Å for the short-range and Coulombic interactions, respectively. This potential has been extensively studied and has been found to offer an excellent description of the structural, dynamical, vibrational, and thermodynamical properties of NS glasses.[10,17,29,31–39] Finally, the potential developed by Jakse *et al.* was used to simulate the CAS glass.[40,41] The cutoff was fixed at 8 and 12 Å for the short-range and Coulombic interactions, respectively. This potential has shown to yield an excellent description of the structural, mechanical, and vibrational properties of CAS glasses.[29,42]

3.3.2 Thermal Cycling Methodology

To assess the degree of reversibility of the glass transition of these systems, all the three glasses were subjected to a thermal cycle, details of which are as follows.[11,43] Starting from well-relaxed liquid configurations, the systems were cooled and subsequently reheated at varying cooling/heating rates (from 100 to 0.1 K/ps, with temperatures steps of 100 K) in the *NPT* ensemble and zero pressure. To filter out any thermal effect, 16 independent configurations were extracted every 1 ps at the end of each temperature step. All configurations were then subjected to an energy minimization in order to compute the enthalpy of their inherent configuration (local ground-state enthalpy).[17,44] All the results presented below are averaged over these 16 configurations. We ensured that the results of the thermal cycling simulations are not affected by any spurious effect of the thermostat and barostat (see **Appendices**).[45]

3.4 Results and Discussion

3.4.1 Features of the Glass Transition

Figure 3. 1 represents the local ground state enthalpy *H* as a function of the temperature *T* (i.e., the enthalpy of the inherent configuration for each temperature). For all systems, *H* decreases monotonically with decreasing temperature. We note that silica (S) has the lowest ground-state enthalpy, which is found between –5515 and –5500 kJ/mol for the studied cooling rates, whereas NS has the highest ground-state enthalpy. Since the enthalpy also reflects at the atomic scale a bond energy density, this result agrees with the fact that S is more polymerized and NS is less polymerized due to the formation of non-bridging oxygen species caused by sodium atoms.[31]

At a certain temperature (the fictive temperature[46] called T_f hereafter), the salient features of the glass transition are recovered and a break in the slope of $H(T)$ is observed for the three glasses. This is an indication that the system can no longer equilibrate over the imposed computational timescale. We, furthermore, note that S and CAS glasses have a sharper transition (given the obvious larger changes in $dH(T)/dT$ across the glass transition), whereas NS exhibits a more gradual transition. When the position of the break in slope is considered (i.e., the fictive temperature), we find that $T_f(\mathrm{S}) > T_f(\mathrm{CAS}) > T_f(\mathrm{NS})$, in agreement with experimental results.[47–49] Further, the fictive temperature decreases with decreasing cooling rate for the three glasses.[46] Overall, the simulations reproduce the generic features of the effect of the cooling rate on the enthalpy across the glass transition.

For S and CAS glass, the local ground state enthalpy $H(T)$ shows a plateau at low temperature and $H(T)$ barely depends on temperature. This signals a weak temperature-dependence of the specific heat. The zero-temperature ground-state enthalpy decreases monotonically with decreasing cooling rate for the three glasses, which is in line with experimental results[10,50] and is simply the indication that the glasses achieved with a lower cooling rate have relaxed toward lower energy values. Conversely, there is no such plateau for the NS glass and a continuous decrease upon decreasing temperature is observed. The suggests that, unlike S and CAS glasses, NS exhibits some more pronounced structural relaxation that lead to a larger enthalpic evolution below T_f. This effect likely results from the higher mobility of the Na atoms, even at low temperature.[51] For instance, we find that, at 800 K (i.e., below T_f), the mobility of the Na atoms

is nearly two orders of magnitude higher than that of all the other species (including Ca atoms, see **Appendices**).[45]

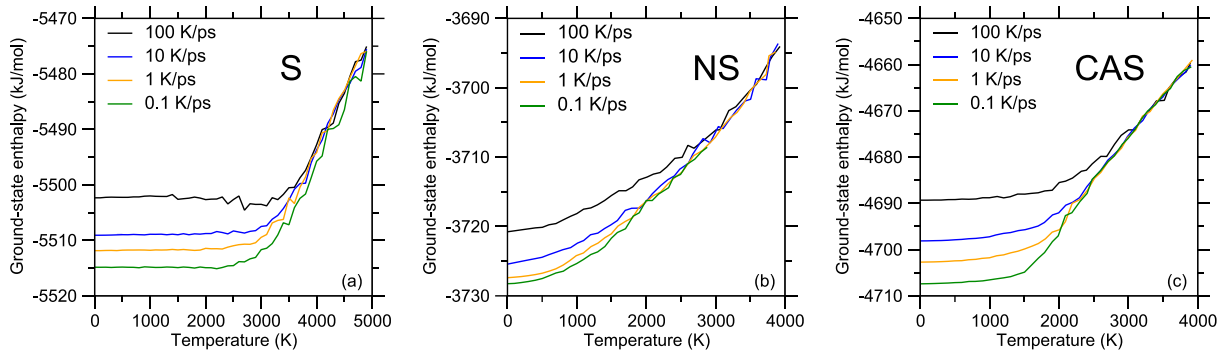

Figure 3. 1 Local ground-state enthalpy $H(T)$ (i.e., enthalpy of the inherent configuration) as a function of temperature T under select cooling rates for **(a)** silica (S), **(b)** sodium silicate (NS), and **(c)** calcium aluminosilicate (CAS). Note that each panel has a different y-axis.

We next focus on the variations in the molar volume V_m (**Figure 3. 2**). For the NS and CAS glasses, the molar volume decreases monotonically with decreasing temperature[52] and a break of slope is also observed around the fictive temperature—although the break of slope is not as sharp as that observed in the case of the local ground-state enthalpy. Note that the break of slope leads to a change in the thermal expansion coefficient at the glass transition.[53] For silica, one notices that the molar volume exhibits an anomalous behavior, that is, a minimum at around 5000 K—in agreement with previous simulations that point to the existence of a liquid-liquid transition in high temperature liquids and their thermodynamic anomalies.[28,54–57] Note that the location of such transitions might be not be directly comparable to our results because of the sensitivity of such transitions to the employed force field. We note that, once in the glassy state, silica exhibits

the lowest extent of thermal expansion, in agreement with experimental results.[3] In general, slower cooling rates result in more compact glasses with lower molar volumes, with the notable exception of silica.[58] NS has the lowest molar volume in general (i.e., more compact), which arises from the fact that Na atoms efficiently fill the empty space within the silicate network.[3] We also note that the cooling rate primarily affects the coefficient of thermal expansion of silica,[54] whereas those of the NS and CAS glasses largely unaffected.[17]

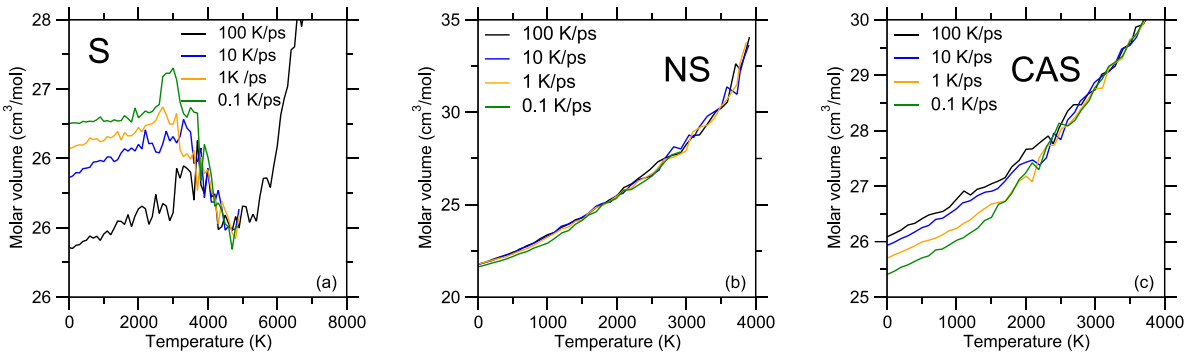

Figure 3. 2 Molar volume as a function of temperature upon select cooling rates for **(a)** silica (S), **(b)** sodium silicate (NS), and **(c)** calcium aluminosilicate (CAS). Note that each panel has a different y-axis.

3.4.2 Effect of the Cooling Rate on the Glass Properties

We now turn our attention to the effect of the cooling rate on the glass properties at zero temperature. A log-log plot of the zero-temperature ground-state enthalpy H as a function of the cooling rate γ suggests a power law dependence, as predicted by mode-coupling theory:[17,59]

$$H(\gamma) = H(\gamma = 0) + (A\gamma)^{1/\delta} \qquad \text{Eq. 18}$$

where A and δ are some fitting parameters, and $H(\gamma = 0)$ is the enthalpy that would be achieved for a (fictitious) zero cooling rate, i.e., after infinitely slow cooling. Note that, in practice, the glass

would necessarily crystalize if cooled infinitely slowly.[2] We find $H(\gamma = 0)$ = –5521, –3731, and –4711 kJ/mol for S, NS, CAS, respectively, which scales well with the degree of polymerization (that is, the higher the glass connectivity, the more energetically stable the glass is).

These parameters are used to calculate the residual enthalpy $\Delta H(\gamma) = H(\gamma) - H(\gamma = 0)$ of the glass at zero temperature as a function of the cooling rate, that is, the increase in enthalpy at 0 K due to a finite cooling rate γ with respect to the one that would be achieved at zero cooling rate. As shown in **Figure 3. 3(a)**, we find that, although the ground-state enthalpy of the three glasses considered herein strongly depends on composition, the dependence on the cooling rate appears to be fairly similar—we find δ = 4.3, 4.7, and 4.1 for the S, NS, and CAS glasses, respectively.

Similarly, we represent in **Figure 3. 3(b)** the molar volume at 0 K, which slightly decreases with decreasing cooling rate for NS and CAS glass. Both systems display an opposite behavior to silica, which exhibits an increase in the molar volume with decreasing cooling rate due its anomalous behavior.[18,54] Overall, we note that the room-temperature molar volume of NS exhibits the lowest dependence on the cooling rate. This likely arises from that, thanks to the high mobility of Na atoms (see Sec. 3a and Supplementary Material),[45] the NS glasses are able to partially continue to relax below their fictive temperature—so that the shift of its fictive temperature upon varying cooling rate only has a limited effect on its final volume. This suggests that such low-temperature volume relaxation might not be controlled by the viscosity of the glass.[60]

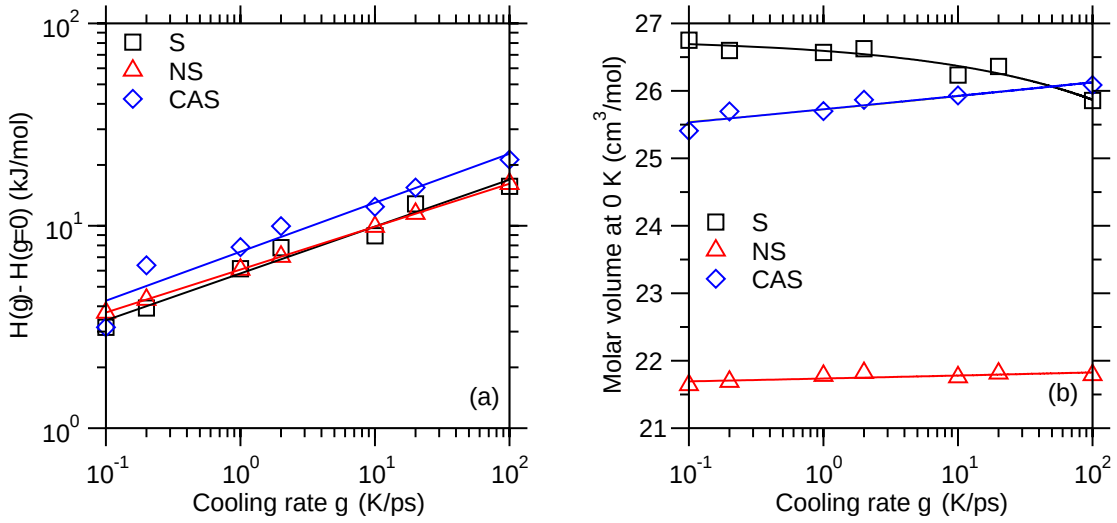

Figure 3. 3 **(a)** Residual enthalpy $\Delta H(\gamma) = H(\gamma) - H(\gamma = 0)$ at 0 K for the silica (S), sodium silicate (NS), and calcium aluminosilicate (CAS) glasses as a function of the cooling rate γ, where $H(\gamma = 0)$ is obtained by fitting $H(\gamma)$ with a power law $H(\gamma) = H(\gamma = 0) + (A\gamma)^{1/\delta}$. The solid lines are power law fits (see Eq. 18). **(b)** Molar volume at 0 K of the three glasses considered herein as a function of the cooling rate. The solid lines are to guide the eye.

3.4.3 Decoupling between Enthalpy and Volume Relaxation

A linear fitting of the high- and low-temperature domains of $H(T)$ or $V_m(T)$ permits one to determine the glass fictive temperature T_f (i.e., as the temperature at which the two linear functions intercept), which, in turn, allows us to substantiate the relationship between T_f and the cooling rate γ (see **Figure 3. 4**). In the case of silica, the fictive temperature is defined as the point at which the molar volume starts to decrease with decreasing temperature. As expected, we note that T_f decreases with decreasing cooling rate γ. This arises from the fact that, upon decreasing cooling rate, the threshold at which the relaxation time of the supercooled liquid exceeds the simulation time (i.e., the point at which the system goes out-of-equilibrium) shifts

toward lower temperatures.[3] However, we note that the fictive temperature determined from the break in slope in $V_m(T)$ is systematically higher than that obtained from the break in slope in $H(T)$ (see **Figure 3. 4**), which is in line with previous simulations conducted for a Lennard-Jones glass.[61] This suggests the existence of a decoupling between enthalpy and volume relaxation, as further discussed below.

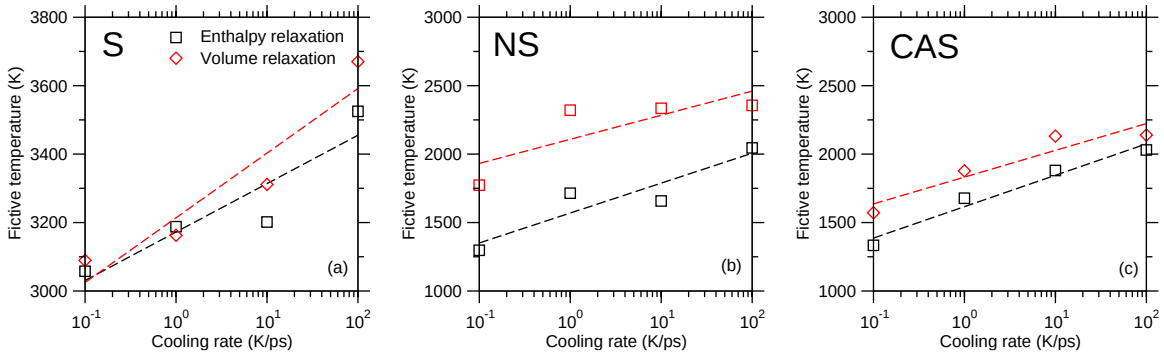

Figure 3. 4 Fictive temperature T_f as a function of the cooling rate γ for the (**a)** silica (S), **(b)** sodium silicate (NS), and **(c)** calcium aluminosilicate (CAS) glasses (calculated from the break in slope of the ground-state enthalpy and molar volume vs. temperature curves, see Figures 3. 1 and 3. 2). The dashed lines are to guide the eye. Note that each panel has a different y-axis.

We now further investigate the distinct features of enthalpy and volume relaxation. Although its applicability has been questioned,[62–64] the Kissinger equation[65,66] can be conveniently used to estimate the apparent activation energy Δh^* of glass transition or structural relaxation:

$$\ln\left(\frac{\gamma}{T_f^2}\right) = \frac{-\Delta h^*}{RT_f} + \text{const} \qquad \text{Eq. 19}$$

where γ is the cooling rate, T_f the fictive temperature, and R the perfect gas constant. Figure 5 shows the Kissinger plots capturing the dependence of the fictive temperature on the cooling rate for the three glasses considered herein. Overall, we note that, despite the statistical fluctuations that are inherent to small simulated systems, the T_f data can be fairly well fitted by the Kissinger equation—both in the case of enthalpy and volume relaxation. **Table 2** presents the apparent activation energy values resulting for the fits (performed by linear regression of the data presented in **Figure 3. 5**). These values are of the same order of magnitude than the apparent activation energy of volume relaxation previously reported for a soda-lime silicate (309 kJ/mol)[66] and a borosilicate glass (615 kJ/mol).[46] Overall, we observe that the apparent activation energy of silica is significantly larger than those of the sodium silicate and calcium aluminosilicate glasses—both for enthalpy and volume relaxation. This is in line with the fact that the NS and CAS glasses are more depolymerized than silica, which facilitates relaxation.

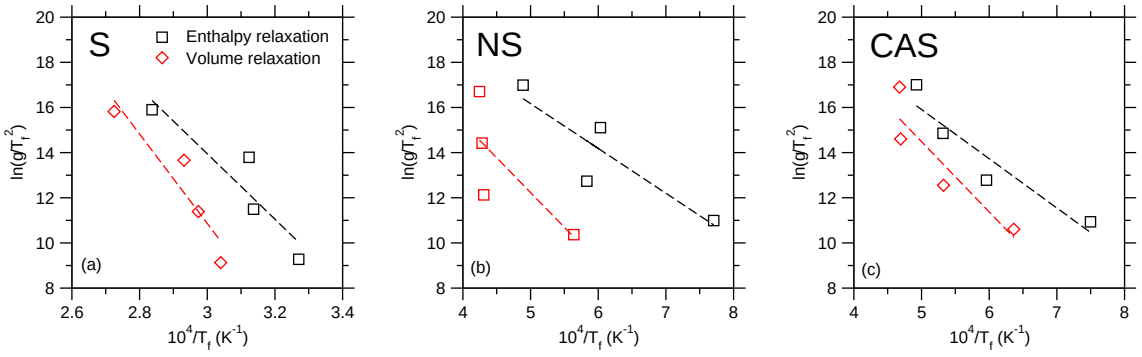

Figure 3. 5 Kissinger plots for the **(a)** silica (S), **(b)** sodium silicate (NS), and **(c)** calcium aluminosilicate (CAS) glasses. The lines are Kissinger fits (Eq. 19), which allow us to estimate an apparent activation energy of enthalpy and volume relaxation (see Table 2).

However, we note that, interestingly, the apparent activation energy associated to volume relaxation is systematically higher than that associated to enthalpy relaxation (by 43-to-65%). This demonstrates the existence of a bifurcation between enthalpy and volume relaxation and suggests they occur via distinct mechanisms. Specifically, our results suggest that volume relaxation is associated to larger energy barriers and, hence, is less kinetically favored than enthalpy relaxation. These observations are in agreement with previous results suggesting that volume relaxation is significantly slower than enthalpy relaxation.[60,67] This was explained from the fact that volume relaxation occurs through long-range reorganizations of the network, whereas enthalpy relaxation occurs through short-range reorganizations.[60,68,69]

Table 2 Apparent activation energies associated to the enthalpy and volume relaxation in the silica, sodium silicate, and calcium aluminosilicate glasses, as obtained by fitting the curves presented in Figure 3. 5 by Eq. 19.

Glass	**Enthalpy relaxation**	**Volume relaxation**
Silica (S)	1200 kJ/mol	1980 kJ/mol
Sodium silicate (NS)	165 kJ/mol	239 kJ/mol
Calcium aluminosilicate (CAS)	181 kJ/mol	259 kJ/mol

3.4.4 Reversibility of the Glass Transition

We now focus on the question of the glass reversibility. Once the glasses have been obtained, we heat the systems back up with the same absolute rate as during the cooling protocol (see **Section 3.3.2**). **Figure 3. 6** represents such cooling/heating cycles across the glass transition. We note

that, upon reheating, the local ground-state enthalpy differs from that obtained upon cooling, which signals the onset of enthalpic relaxation—as observed experimentally or also evidenced from kinetic constraint models.[70] More specifically, the decrease in the local ground-state enthalpy explored upon reheating indicates that the glass has, indeed, relaxed toward a lower energy state. This feature is compatible with the "overshoot" that is typically observed in calorimetry experiments.[71] However, it is seen that such a behavior is strongly system-dependent. For instance, for a given heating/cooling rate (e.g., 1 K/ps), silica (S) displays a larger hysteresis curve when compared to the NS or CAS systems.

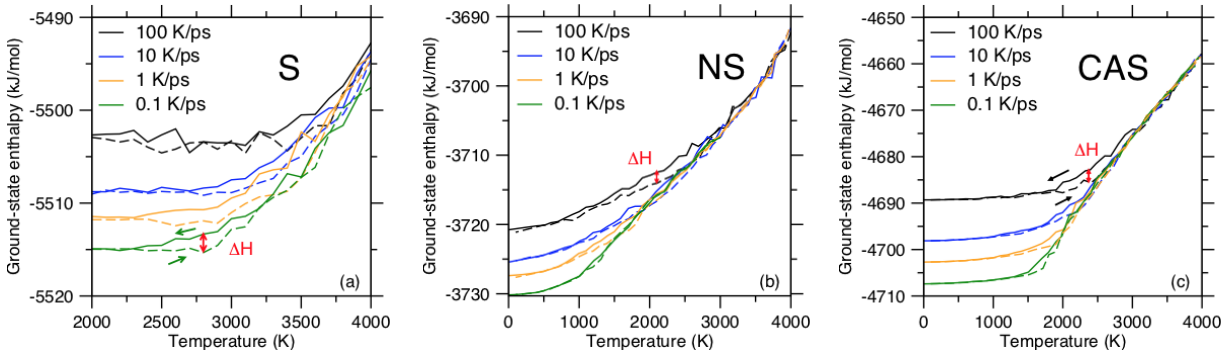

Figure 3. 6 Local ground-state enthalpy $H(T)$ (i.e., enthalpy of the inherent configuration) as a function of temperature under select cooling/reheating rates for **(a)** silica (S), **(b)** sodium silicate (NS), and **(c)** calcium aluminosilicate (CAS) glasses. The solid (same as Figure 3. 1) and dashed curves refer to the cooling and heating simulations, respectively. Note that each panel has a different y-axis.

3.4.5 Glass Relaxation at the Vicinity of the Glass Transition

In order to further quantify the enthalpy relaxation as a function of temperature, we calculate the enthalpy relaxation $\Delta H = H_{cool}(T) - H_{heat}(T)$, which is here defined, at fixed cooling/reheating rate, as the ground-state enthalpy difference between the cooling and the heating curves. **Figure 3. 7** represents such quantity for the three systems at different cooling/heating cycles. It is interesting to note that the temperature at which enthalpic relaxation is maximum (i.e. the maximum of ΔH in **Figure 3. 7**) is close to the fictive temperature and this typical temperature exhibits qualitatively the same dependence on the cooling rate as that of T_f, i.e., it decreases with decreasing cooling rate. This can be understood from the following. At high temperature ($T \gg T_f$), no relaxation is observed since the typical relaxation time is several orders of magnitude lower (picoseconds) than the typical simulation time. As such, the system is at (metastable) equilibrium with no thermodynamic driving force for relaxation. Therefore, the liquid tracks the imposed temperature variation (i.e., $\Delta H = 0$). On the other hand, at low temperature ($T \ll T_f$), relaxation is barely observed because the dynamics is too slow with a large viscosity and relaxation that is kinetically frozen. This is related to the fact that the glass is trapped in some local minimum in the enthalpy landscape (characterized by $H_{cool}(\gamma)$) and, as a result, the system follows instantaneously the imposed temperature change (i.e., $\Delta H = 0$). Eventually, relaxation can only occur around $T = T_f$, that is, when the relaxation time becomes comparable to the typical observation time.

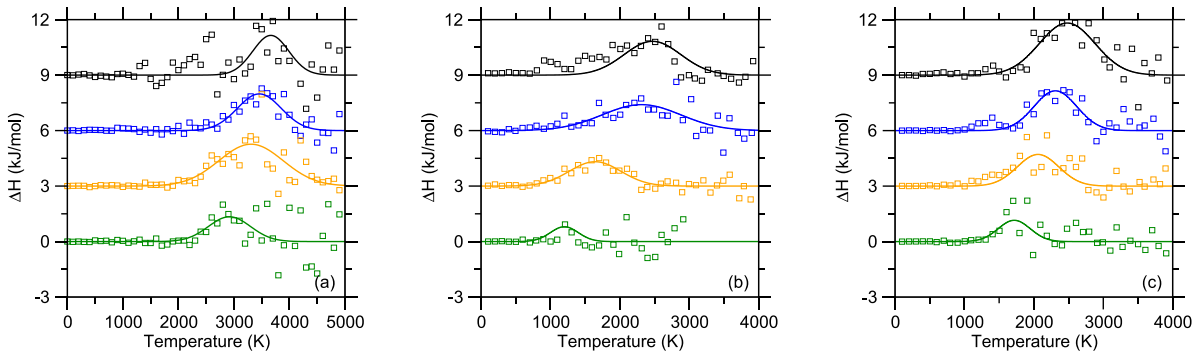

Figure 3. 7 Relaxation enthalpy (i.e., difference of ground-state enthalpy upon cooling and reheating) as a function of temperature for **(a)** silica (S), **(b)** sodium silicate (NS), and **(c)** calcium aluminosilicate (CAS) glasses. The solid lines are Gaussian fits. The values are vertically shifted for clarity. The cooling/reheating rates are (from top to bottom) 100, 10, 1, and 0.1 K/ps.

We further describe the relaxation dynamics by fitting the decrease in enthalpy induced by relaxation with a Gaussian function:

$$\Delta H = \Delta H_{\max} \exp\left[\frac{-(T-T_{\max})^2}{2\Delta T^2}\right] \qquad \text{Eq. 20}$$

wherein $T_{\max}$ represents the temperature where relaxation is maximum, $\Delta H_{\max}$ the maximum extent of enthalpy relaxation, and ΔT the typical temperature range over which relaxation occurs. Note that $\Delta H(T)$ is not fully symmetric with respect to $T_{\max}$ so that a Gaussian function may not offer the best fit (and may not have a clear physical origin). However, the goal of the present fit is only to extract these three relevant fitting parameters. To avoid any spurious effect of the high-temperature fluctuations observed in **Figure 3. 7** on the outcome of the fit, we apply on the data a weighting factor $w = 1/T$ (where T is the temperature) during the fitting procedure. This allows us to place more emphasis on the low-temperature data (which exhibit lower

uncertainty). At the highest cooling/heating rate (100 K/ps), we obtain ΔH_{max} = 2.1, 1.8, and 2.9 kJ/mol for the S, NS, and CAS glasses, respectively. The dependence of the three metrics yielded by the fit on the cooling/heating rate is described in the following (**Figure 3. 8**).

For all the glasses considered in the present contribution, T_{max} decreases with decreasing cooling/reheating rate (**Figure 3. 8(a)**). The value of T_{max} is very close to the fictive temperature and exhibits a similar dependence on the cooling rate—as also determined recently.[72] We furthermore note that, in the case of the sodium silicate glass, an extrapolation of $T_{max}(\gamma)$ toward lower cooling rates values (typically 1 K/s) leads to a value that is comparable to the glass transition temperature observed experimentally (see Ref. [17]). The T_{max} of S is overall higher than the T_{max} of NS and CAS—a result that is also consistent with the experimental observations, i.e., S has the highest T_g, which is reduced once depolymerization is produced by the addition of modifiers as it is the case for NS and CAS.[3]

The maximum enthalpy relaxation (ΔH_{max}) decreases with decreasing cooling rate for the three glasses (**Figure 3. 8(b)**). The origin of this trend is illustrated in **Figure 3. 9** and is explained in the following. Slower cooling rates result in more relaxed (i.e., more stable) glasses (see **Figures 3. 1** and **3. 3(a)**). However, slower heating rates provide more time to the formed glass to further relax upon reheating. **Figure 3. 9** shows the typical shape of the stretched-exponential relaxation of a glass in isothermal condition. The black arrows indicate the extent of enthalpy relaxation that can be achieved upon cooling and, then, reheating. Note that, since the cooling and heating rates are equal to each other, the times over which the system is able to relax at a given

temperature upon cooling and subsequent reheating are the same. However, due to the stretched-exponential nature of glass relaxation, the extent of relaxation achieved upon reheating is lower than that achieved upon cooling. The red arrows now indicate the relaxation that can be achieved upon slower cooling and reheating. It can be observed that, although the observation (simulation) time increases, the actual extent of enthalpy relaxation is lower than upon faster cooling/reheating. As such, varying the cooling/heating rate can be used to describe the relaxation dynamics at different stages, namely, early-stage relaxation for high cooling/heating rates and longer-term relaxation for lower cooling/heating rates (see **Figure 3. 9**). Hence, that fact that $\Delta H_{\max}$ decreases with decreasing cooling/heating rate indicates that most of the relaxation occurs at early-stage and that the relaxation dynamics subsequently slows down, consistently with the stretched-exponential nature of glass relaxation).[15,60,67,68,73,74] Overall, we find that NS has the smallest $\Delta H_{\max}$. This may arise from the high mobility of the Na atoms, which allows some significant relaxation to occur during the cooling phase at $T < T_f$.

Finally, we place our attention on ΔT (see **Figure 3. 8(c)**). ΔT can be considered as being the extent of temperature over which relaxation can occur, that is, over which the relaxation time of the glass is high enough (i.e., otherwise the system would have already fully relaxed upon cooling and would be at equilibrium), but not too high (i.e., otherwise relaxation would be too slow to be observed at all within the timescale of our simulation)—i.e., ΔT is the range of temperature for which the relaxation time is high enough for the system to be out-of-equilibrium, but low enough for relaxation to be kinetically allowed. Hence, relaxation is only observed when the relaxation time of the glass becomes comparable to that of our simulation time. Based on

this, the extent of temperature over which the relaxation time is comparable to the simulation time should be controlled by the derivative of the relaxation time with respect to temperature (i.e., the glass fragility).[75] Since the viscosity (and relaxation time) increases exponentially with decreasing temperature, we would expect, upon decreasing cooling rate, the extent of the temperature window over which the relaxation time is comparable to the simulation time should decrease. This should result in a more well-defined glass transition (i.e., lower ΔT) upon decreasing cooling rate. Although such a trend is partially verified for the NS and CAS glasses (see **Figure 3. 8(c)**), the fluctuations in the data do not allow us to conclusively confirm this behavior. The relationship between ΔT and glass fragility is also in agreement with the fact that we find silica to exhibit the largest ΔT, in agreement with its low fragility value.[76]

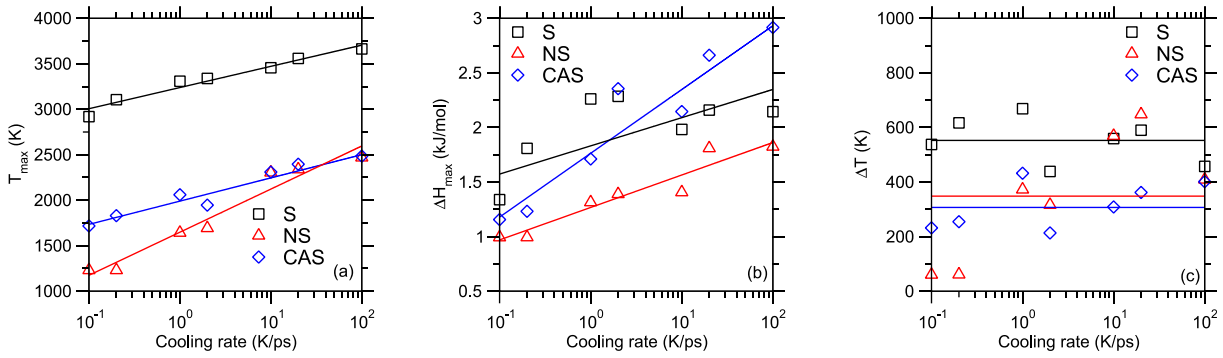

Figure 3. 8 **(a)** Temperature at which the enthalpy relaxation is maximum (T_{max}), **(b)** maximum extent of enthalpy relaxation (ΔH_{max}), and **(c)** typical range of temperature over which enthalpy relaxation occurs (ΔT) as a function of the cooling/heating rate for silica (S), sodium silicate (NS), and calcium aluminosilicate (CAS). The lines are to guide the eye.

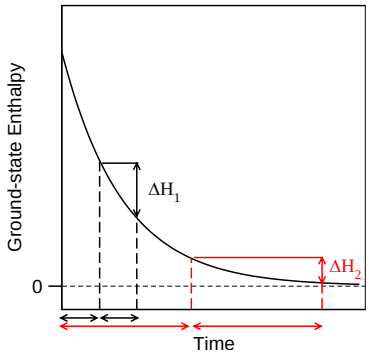

Figure 3. 9 Schematic showing the typical stretched-exponential enthalpy relaxation of a glass in isothermal conditions. The arrows indicate the extent of relaxation that can be achieved between cooling and subsequent reheating in the case of (black) fast cooling/heating and (red) slow cooling/heating.

3.5 Conclusions

In summary, we have studied relaxation and glass transition reversibility in three archetypical silicate glasses by means of molecular dynamics simulations. Overall, the simulations reproduce the generic features of the glass transition and of its dependence on the cooling rate. This analysis confirms that the glass ground-state enthalpy (i.e., the position locally occupied by the glass within the enthalpy landscape) exhibits a power-law dependence on the cooling rate, in agreement with mode-coupling theory. Based on these simulations, a systematic bifurcation between enthalpy and volume relaxation is evidenced, which suggests that they occur via distinct mechanisms. Finally, based on a novel methodology combining thermal cycles and inherent configuration analysis, we characterize the degree of (ir)reversibility of the glass transition. We find that both the extent of irreversibility and the range of temperature over which relaxation

occurs are strongly system-specific. Overall, the present results provide a numerical assessment of the calorimetric glass transition using MD simulations, and should permit to investigate in the future the effect of composition or pressure on glass relaxation.

3.6 Appendices

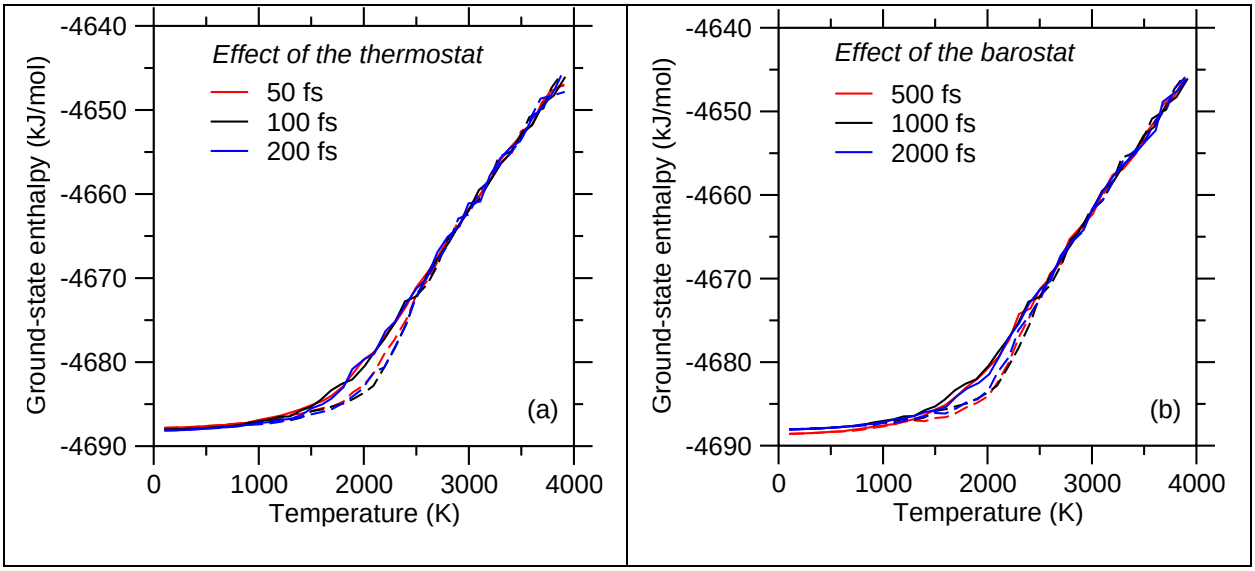

Figure A 1 Local ground-state enthalpy of a CAS glass as a function of temperature (with a cooling/heating rate of 1K/ps) for select **(a)** thermostat and **(b)** barostat relaxation times.

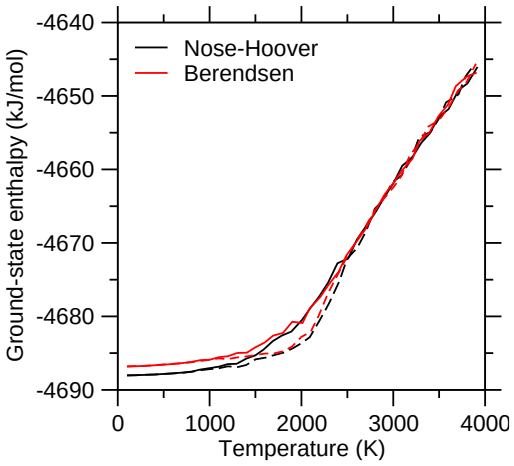

Figure A 2 Local ground-state enthalpy of a CAS glass as a function of temperature (for a cooling/heating rate of 1K/ps) obtained with the Nosé–Hoover and Berendsen thermostat/barostats.

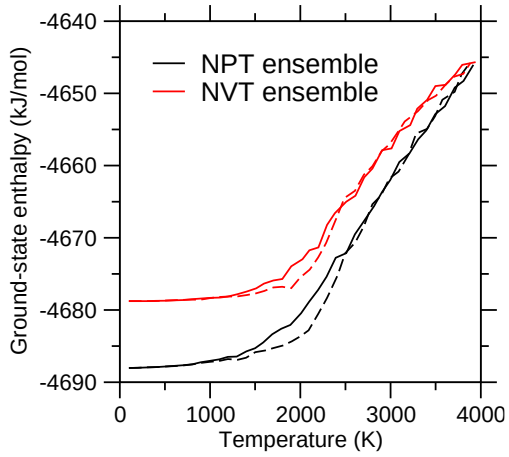

Figure A 3 Local ground-state enthalpy of a CAS glass as a function of temperature (for a cooling/heating rate of 1K/ps) obtained with the Nosé–Hoover thermostat in the *NPT* and *NVT* ensembles.

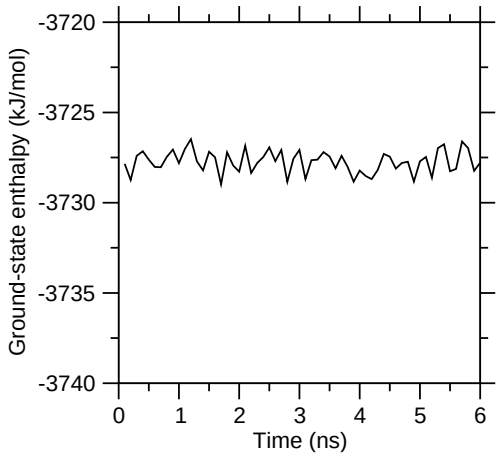

Figure A 4 Local ground-state enthalpy of a NS glass (after cooling at 1K/ps) as a function of time at 300K.

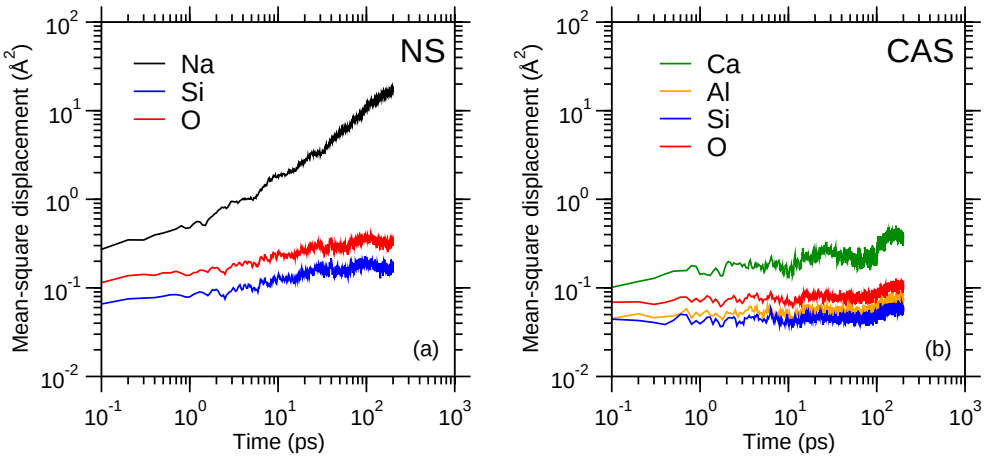

Figure A 5 Mean-square displacement of each element at 750K in **(a)** NS and **(b)** CAS glasses.

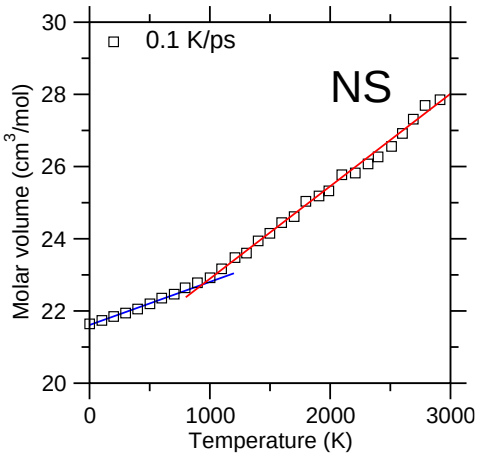

Figure A 6 Ground-state enthalpy *H(T)* of an NS glass upon cooling at 0.1K/ps. The low- and high-temperature domains of *H(T)* are fitted by some linear functions to identify the fictive temperature.

3.7 References

[1] P.G. Debenedetti and F.H. Stillinger, Nature **410**, 259 (2001).

[2] E.D. Zanotto and J.C. Mauro, J. Non-Cryst. Solids **471**, 490 (2017).

[3] A.K. Varshneya, *Fundamentals of Inorganic Glasses* (Academic Press Inc, 1993).

[4] M.M. Smedskjaer, M. Bauchy, J.C. Mauro, S.J. Rzoska, and M. Bockowski, J. Chem. Phys. **143**, 164505 (2015).

[5] M. Wang, B. Wang, T.K. Bechgaard, J.C. Mauro, S.J. Rzoska, M. Bockowski, M.M. Smedskjaer, and M. Bauchy, J. Non-Cryst. Solids **454**, 46 (2016).

[6] O. Gulbiten, J.C. Mauro, X. Guo, and O.N. Boratav, J. Am. Ceram. Soc. **101**, 5 (2017).

[7] Y.-Z. Yue, J. Non-Cryst. Solids **354**, 1112 (2008).

[8] J. Jackle, Rep. Prog. Phys. **49**, 171 (1986).

[9] Ellison Adam and Cornejo Iván A., Int. J. Appl. Glass Sci. **1**, 87 (2010).

[10] M. Bauchy and M. Micoulaut, Nat. Commun. **6**, 6398 (2015).

[11] B. Mantisi, M. Bauchy, and M. Micoulaut, Phys. Rev. B **92**, 134201 (2015).

[12] C. Massobrio, J. Du, M. Bernasconi, and P.S. Salmon, editors , *Molecular Dynamics Simulations of Disordered Materials* (Springer International Publishing, Cham, 2015).

[13] C. Yildirim, J.-Y. Raty, and M. Micoulaut, J. Chem. Phys. **144**, 224503 (2016).

[14] P. Boolchand and B. Goodman, MRS Bull. **42**, 23 (2017).

[15] M. Micoulaut, Rep. Prog. Phys. **79**, 066504 (2016).

[16] J. Du, in *Mol. Dyn. Simul. Disord. Mater.*, edited by C. Massobrio, J. Du, M. Bernasconi, and P.S. Salmon (Springer International Publishing, 2015), pp. 157–180.

[17] X. Li, W. Song, K. Yang, N.M.A. Krishnan, B. Wang, M.M. Smedskjaer, J.C. Mauro, G. Sant, M. Balonis, and M. Bauchy, J. Chem. Phys. **147**, 074501 (2017).

[18] K. Vollmayr, W. Kob, and K. Binder, Phys. Rev. B **54**, 15808 (1996).

[19] Y. Guissani and B. Guillot, J. Chem. Phys. **98**, 8221 (1993).

[20] M. Bauchy, B. Guillot, M. Micoulaut, and N. Sator, Chem. Geol. **346**, 47 (2013).

[21] R.C. Welch, J.R. Smith, M. Potuzak, X. Guo, B.F. Bowden, T.J. Kiczenski, D.C. Allan, E.A. King, A.J. Ellison, and J.C. Mauro, Phys. Rev. Lett. **110**, 265901 (2013).

[22] Mauro John C., Ellison Adam J., and Pye L. David, Int. J. Appl. Glass Sci. **4**, 64 (2013).

[23] S. Plimpton, J. Comput. Phys. **117**, 1 (1995).

[24] S. Nosé, Mol. Phys. **52**, 255 (1984).

[25] W.G. Hoover, Phys. Rev. A **31**, 1695 (1985).

[26] B.W.H. van Beest, G.J. Kramer, and R.A. van Santen, Phys. Rev. Lett. **64**, 1955 (1990).

[27] F. Yuan and L. Huang, Sci. Rep. **4**, 5035 (2014).

[28] K. Vollmayr, W. Kob, and K. Binder, Phys. Rev. B **54**, 15808 (1996).

[29] B. Wang, Y. Yu, Y.J. Lee, and M. Bauchy, Front. Mater. **2**, (2015).

[30] J. Horbach and W. Kob, Phys. Rev. B **60**, 3169 (1999).

[31] J. Du and A.N. Cormack, J. Non-Cryst. Solids **349**, 66 (2004).

[32] M. Bauchy, J. Chem. Phys. **137**, 044510 (2012).

[33] J. Du and L.R. Corrales, Phys. Rev. B **72**, 092201 (2005).

[34] A. Pedone, G. Malavasi, A.N. Cormack, U. Segre, and M.C. Menziani, Chem. Mater. **19**, 3144 (2007).

[35] M. Bauchy and M. Micoulaut, Phys. Rev. B **83**, 184118 (2011).

[36] M. Bauchy, B. Wang, M. Wang, Y. Yu, M.J. Abdolhosseini Qomi, M.M. Smedskjaer, C. Bichara, F.-J. Ulm, and R. Pellenq, Acta Mater. **121**, 234 (2016).

[37] M. Bauchy and M. Micoulaut, EPL Europhys. Lett. **104**, 56002 (2013).

[38] B. Wang, Y. Yu, M. Wang, J.C. Mauro, and M. Bauchy, Phys. Rev. B **93**, 064202 (2016).

[39] M. Micoulaut and M. Bauchy, Phys. Rev. Lett. **118**, 145502 (2017).

[40] M. Bouhadja, N. Jakse, and A. Pasturel, J. Chem. Phys. **138**, 224510 (2013).

[41] N. Jakse, M. Bouhadja, J. Kozaily, J.W.E. Drewitt, L. Hennet, D.R. Neuville, H.E. Fischer, V. Cristiglio, and A. Pasturel, Appl. Phys. Lett. **101**, 201903 (2012).

[42] M. Bauchy, J. Chem. Phys. **141**, 024507 (2014).

[43] M. Bauchy and M. Micoulaut, Nat. Commun. **6**, 6398 (2015).

[44] N.M.A. Krishnan, B. Wang, Y. Yu, Y. Le Pape, G. Sant, and M. Bauchy, Phys. Rev. X **7**, 031019 (2017).

[45] See Supplemental Material at [URL will be inserted by publisher] for more details about the molecular dynamics simulations conducted herein.

[46] C.T. Moynihan, A.J. Easteal, M.A. De BOLT, and J. Tucker, J. Am. Ceram. Soc. **59**, 12 (1976).

[47] A. Agarwal, K.M. Davis, and M. Tomozawa, J. Non-Cryst. Solids **185**, 191 (1995).

[48] Agarwal Anand and Tomozawa Minoru, J. Am. Ceram. Soc. **78**, 827 (2005).

[49] J.F. Stebbins, E.V. Dubinsky, K. Kanehashi, and K.E. Kelsey, Geochim. Cosmochim. Acta **72**, 910 (2008).

[50] N. Giovambattista, C.A. Angell, F. Sciortino, and H.E. Stanley, Phys. Rev. E **72**, 011203 (2005).

[51] M. Bauchy and M. Micoulaut, Phys. Rev. B **83**, 184118 (2011).

[52] J.C. Mauro and M.M. Smedskjaer, J. Non-Cryst. Solids **396**–**397**, 41 (2014).

[53] A.Q. Tool, J. Am. Ceram. Soc. **29**, 240 (1946).

[54] J.M.D. Lane, Phys. Rev. E **92**, 012320 (2015).

[55] J.L. Barrat, J. Badro, and P. Gillet, Mol. Simul. **20**, 17 (1997).

[56] M. Micoulaut, Chem. Geol. **213**, 197 (2004).

[57] M.S. Shell, P.G. Debenedetti, and A.Z. Panagiotopoulos, Phys. Rev. E **66**, 011202 (2002).

[58] R. Brückner, J. Non-Cryst. Solids **5**, 123 (1970).

[59] W. Kob and H.C. Andersen, Phys. Rev. E **51**, 4626 (1995).

[60] Y. Yu, M. Wang, M.M. Smedskjaer, J.C. Mauro, G. Sant, and M. Bauchy, Phys. Rev. Lett. **119**, 095501 (2017).

[61] K. Vollmayr, W. Kob, and K. Binder, J. Chem. Phys. (1998).

[62] R. Svoboda, J. Therm. Anal. Calorim. **118**, 1721 (2014).

[63] R.L. Blaine and H.E. Kissinger, Thermochim. Acta **540**, 1 (2012).

[64] R. Svoboda, P. Čičmanec, and J. Málek, J. Therm. Anal. Calorim. **114**, 285 (2013).

[65] H.E. Kissinger, Anal. Chem. **29**, 1702 (1957).

[66] O.S. Narayanaswamy, J. Am. Ceram. Soc. **54**, 491 (1971).

[67] Y. Yu, M. Wang, D. Zhang, B. Wang, G. Sant, and M. Bauchy, Phys. Rev. Lett. **115**, 165901 (2015).

[68] M. Potuzak, R.C. Welch, and J.C. Mauro, J. Chem. Phys. **135**, 214502 (2011).

[69] N.M.A. Krishnan, B. Wang, Y. Le Pape, G. Sant, and M. Bauchy, Phys. Rev. Mater. **1**, 053405 (2017).

[70] M. Micoulaut, J. Phys.-Condens. Matter **22**, (2010).

[71] P. Badrinarayanan, W. Zheng, Q. Li, and S.L. Simon, J. Non-Cryst. Solids **353**, 2603 (2007).

[72] D.S. Sanditov and M.I. Ojovan, Phys. B Condens. Matter **523**, 96 (2017).

[73] Y. Yu, J.C. Mauro, and M. Bauchy, ArXiv180101969 Cond-Mat (2018).

[74] J.C. Phillips, Rep. Prog. Phys. **59**, 1133 (1996).

[75] C.A. Angell and others, Science **267**, 1924 (1995).

[76] R. Böhmer, K.L. Ngai, C.A. Angell, and D.J. Plazek, J. Chem. Phys. **99**, 4201 (1998).